May 2013

Development of a Novel Revison Total Hip Arthroplasty Method for Femoral Component Extraction

Michael Kevin Keenan
University of Wisconsin-Milwaukee

DEVELOPMENT OF A NOVEL REVISON TOTAL HIP ARTHROPLASTY METHOD FOR FEMORAL COMPONENT EXTRACTION

by

Michael Keenan

A Thesis Submitted in

Partial Fulfillment of the

Requirements for the Degree of

Masters of Science

in Engineering

at

The University of Wisconsin-Milwaukee

May 2013

ABSTRACT

DEVELOPMENT OF A NOVEL REVISON TOTAL HIP ARTHROPLASTY
METHOD FOR FEMORAL COMPONET EXTRACTION
by

Michael Keenan

The University of Wisconsin-Milwaukee, 2013
Under the Supervision of Professor Jill Meyer

Revision total hip arthroplasty is an expensive, arduous procedure where a femoral implant must first be removed and then replaced. The most difficult part of this procedure is the removal of the hip implant, without damaging the host bone. To make this process easier, it is proposed that a device could utilize an implant's natural frequency to propagate cracks in the bone cement used to bond the implant to the host bone. The foci of this thesis is to (i) determine the natural frequency of an implant, (ii) design a device that can be easily used in a surgical setting while efficiently transferring vibration energy into an implant, and (iii) show that the vibrational energy can be used to propagate cracks in the cement mantel. To validate these foci both *in-silico* and *in-vitro* methods have been used. *In-silico* models have been designed to determine an implant's natural frequency and to show that low amplitude mechanical vibrations can be used to propagate cracks in the cement mantel. In the *in-vivo* study an initial design has been proposed and successfully prototyped and calibrated to output vibrations to the proper frequency. In order to keep the proposed design safe for surgical use, it has been designed such that internal stresses are less than the yielding stress of bone, and in order to facilitate crack propagation, the crack must first be externally nucleated by the operator.

TABLE OF CONTENTS

LIST OF FIGURES

LIST OF TABLES

NOMENCLATURE

CT - Computed Tomography

CZM - Cohesive Zone Method

d - depth

E - Modulus of Elasticity

F - Force

f - Frequency

f_o^E - Natural Frequency for a Desired Mode and Boundary Condition with a Density of 2000kg/m^3

f_o^ρ - Natural Frequency for a Desired Mode and Boundary Condition with a Modulus of Elasticity of 116GPa

FE - Finite Element

FEM - Finite Element Method

I - Mass Moment of Inertia

IR - Infrared

K - Stress Concentration Factor

K_{1C} - Fracture Toughness for Mode 1

l - Length

m - Mass

PMMA - Polymethyl Methacrylate

r - Radius

r_α - Time Decaying Radius

rTHA - Revision Total Hip Arthroplasty

T - Torque

t - Time

THA - Total Hip Arthroplasty

w - Width

x - Position perpendicular to y

XFEM - Extended Finite Element Method

y - Position perpendicular to x

α - Dampening Constant

ε - Strain

ζ - Dampening Ratio

θ - Angle

θ_{α} - Frequency of Overshoot

μ - Coefficient of Friction

ν - Poisson's Ratio

ρ - Density

σ - Stress

σ_1 - Maximum Principal Stress

σ_{Bulk} - Bulk Stress

σ_y - Yield Stress

τ - Shear Stress

ACKNOWLEDGEMENTS

First and foremost, I would like to give thanks to my principle investigator and graduate adviser Dr. Jill Meyer. She gave me the opportunity to grow as a student, a researcher and to grow professionally by working individually on a product development project. While executing this project, she gave me the freedom to learn by trial and error in addition to being a constant source of motivation. She has always pushed me to do my best and to aim for a level of excellency in research and teaching, which I had not previously attained. Without her support this project would not have been possible.

The research performed in this thesis would not have been possible without all of my collaborators. I would like to thank Dr. Matthew Squire, for providing the motivation behind the project as well as proposing the initial project concept. One graduate student also provided the support in electrical engineering necessary to perform the device calibration seen in this document. I would like to thank Kevin Staniszewski, for his support in this role. I would also like to take the opportunity to thank the members of the UWM engineering machine shop, for their knowledge and support in choosing materials, and building the prototyped device.

Last, but certainly not least, I would like to take the opportunity to thank my family. Without their support I would not have been able to complete this research and necessary course work. Specifically I would like to thank Tom Keenan, for all the car rides, John Keenan for showing me how to relax when things got tough. I would like to thank Marie, Thorsten, William and Layla Leucker for their continued support and help. Finally, I would like to thank my parents Kevin and Sharon Keenan, whom supported me in the transition from an undergraduate to graduate student and always believed I could finish anything I started.

CHAPTER 1 BACKGROUND

1.0 Introduction

In this chapter the basic background knowledge necessary to comprehend the remainder of this thesis is offered. The focus of this thesis is to develop a device for surgical use in a revision hip replacement surgery. For this reason design is based on both biology and engineering so a multi-disciplinary background is necessary for the evaluation of this research. In this chapter an introduction to anatomy is offered in Section 1.1, Section 1.2 discusses total hip arthroplasty (THA) or hip replacement surgery. A brief overview of engineering mechanics in supplied in Section 1.3 and finally an overview of vibrations is offered in Section 1.4.

1.1 Anatomy

The part of the body of focus in this thesis is the femur, this is the bone located in the thigh. The femur consists of several parts, the femoral head, the femoral neck and the femur shaft, or diaphysis. The femoral head is the component of the femur which connects the thigh to the hip. Next the femoral neck connects the femoral head to the femur shaft. These features are shown in Figure 1.

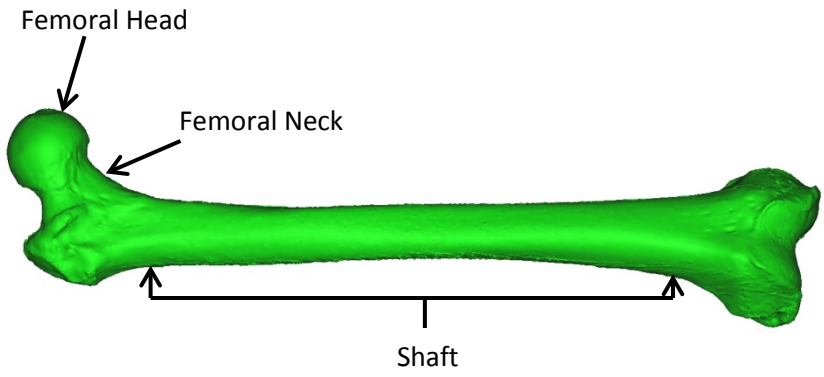

Figure 1: Parts of the Femur.
Shown here are the different components of the femur.

Next it is important to be able to describe anatomical directions and planes in a way similar to a Cartesian coordinate system. A Cartesian coordinate system can be placed on the body where X is directed forward, Y pointed upwards and Z is perpendicular to X and Y directed

to the right, as shown in Figure 2. The human body can be described by a set of three planes: the transverse plane, sagittal plane and frontal plane. The transverse (or axial plane) is a plane that splits the body into upper and lower segments (or the X-Z plane). Next is the sagittal plane, this divides the body into left and right segments (or X-Y plane). Lastly is the frontal plane which divides the body into front and back segments (or Y-Z plane).

Direction is also described by another set of key terms. A point that is directed backwards (-X) on the transverse plane is coined posterior, while a point directed forward (+X) on the transverse plane is called anterior. Points nearer to the middle of the body on the frontal plane are called medial, while lateral points are those who are further from the middle of the body. On the axial plane, points directed upwards (+Y) are superior, while points directed downwards (-Y) are inferior. Figure 2 shows all the anatomical planes and directional terms on the human body.

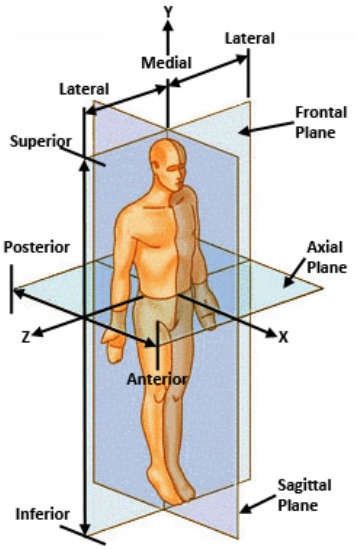

Figure 2: Anatomical Planes and Directional Terms [1].
Described in this figure is the different anatomical planes, and directions.

1.2 Total Hip Arthroplasty

Total hip arthroplasty (THA) is a process where the femoral head and neck are removed and replaced with an artificial implant. A THA is most commonly performed due to severe pain caused by arthritis, or a fracture of the femoral neck. In recent years THA has become a more common place procedure where 285,000 THA's are performed each year. It is estimated that by 2030 the number of THA's performed each year will increase to 575,000 [2]. The surgery typically takes up to an hour and a half and requires both surgical skill and expertise. Two types of implants are commonly used: smooth implants and porous coated implants. A smooth implant is bonded to the host bone with bone cement while a porous coated implant is press fit into the host bone, and boney ingrowth is used to establish fixation. The components of a THA include the femoral stem with a femoral head, and an acetabular cup, as shown in Figure 3. Once the operation is complete, hospital discharge time for the patient is typically between a few days upward to 40 days [3, 4].

In 17.5% of cases an implant will need to be replaced, due to loosening of the implant, infection, or failure of the implant [2]. The surgical procedure to replace the implant is called a revision total hip arthroplasty (rTHA) and follows a similar procedure as a THA but requires a technically challenging process to first remove the previously implanted components. Removing the implant is a difficult task which requires a highly specialized and skilled surgeon. Because of the technically challenging procedure only a select number of orthopedic surgeons that perform primary THAs perform rTHAs. The process for removing the implant is an exceedingly invasive process with longer operation times. The net result is that an rTHA is a more costly procedure, requires a more skilled surgeon and takes a longer amount of time for patient recovery.

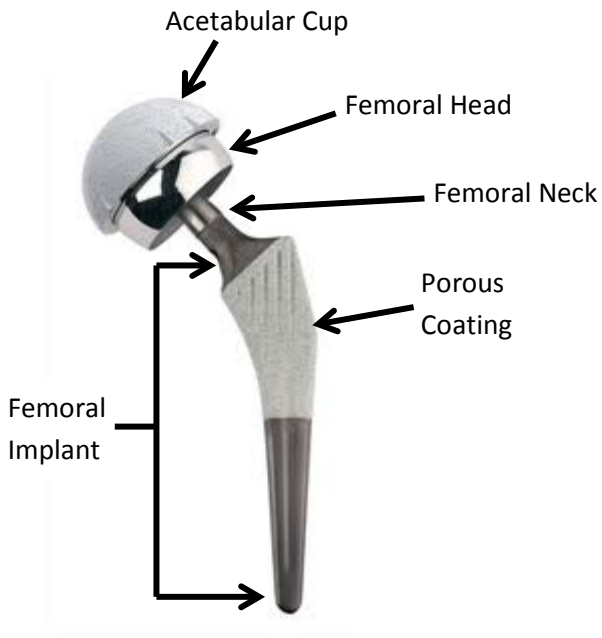

Figure 3: Hip Replacement Implant Components.
Like the components of a hip, a hip implant also consists of several components. This figure shows the components of the implant.

1.3 Engineering Mechanics

Engineering mechanics is a broad field where the response of a system to an external load is studied. One of the most fundamental principles in engineering mechanics is the evaluation of stress (σ), or force per unit area. For example if you have two paper clips, one smaller and one larger and apply the same force to both of them, the smaller one will deform more than the larger one. This is because the cross sectional area for which the force is distributed is smaller for the small paper clip, causing larger stresses, which correlates to larger deformation.

Deformation of a system in mechanics is described by strain (ϵ). Strain is mathematically described as the change in length divided by the original length. Stress and strain can be plotted against each other as shown in Figure 4 [5]. The stress-strain curve is divided into two regions, an elastic region and a plastic region. In the elastic region, when all stress is removed from the system the object returns to its original shape, just like an elastic rubber band. Additionally in the elastic zone, stress and strain are linearly related by the modulus of elasticity (E). The end of the elastic zone is marked by the yield stress (σ_y). Once the yield stress has been surpassed some level of permanent deformation occurs like with a twist tie; this region is known as the plastic zone.

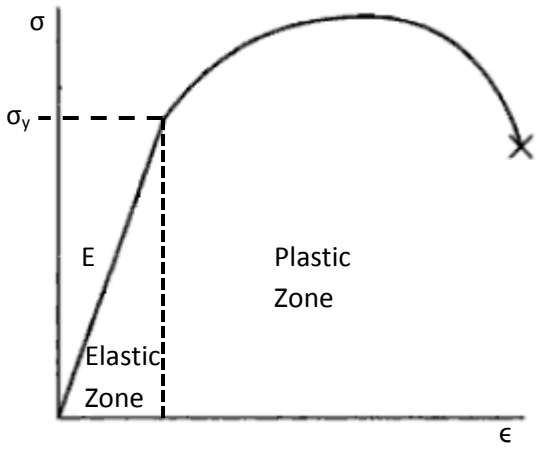

Figure 4: Typical Engineering Stress Strain Curve.
Shown here is a typical engineering stress strain curve. The elastic zone is an area where deformation is not permanent. The elastic zone ends at the yield stress (σ_y) and the plastic zone starts. In the plastic zone, deformation is permanent.

Up to this point stress has been defined as the force divided by the area to which it is applied. In this context the force is perpendicular or normal to the area, when a force is not normal to the area, then the stress is said to be in shear (τ). By combining normal and shear stresses any system of stresses can be described. Additionally materials behave different at the surface or at complex geometrical areas in comparisons to the overall or bulk material. Stresses that are observed by the bulk material are denoted as (σ_{Bulk}). Within the bulk material it is possible to adjust the volume of interested such that a state of stress is achieved with no shear stress; this is known as a state of principle stresses. Principle stresses are denoted as σ_1, σ_1, and σ_3 where σ_1 is always the largest and σ_3 is always the smallest value. In order to determine the principle stresses of a system the area for which you evaluate the stresses is rotated. This is demonstrated in Figure 5 with a 2D example, were the region of interest is rotated and the shear stresses fall to zero and the principle stresses are determined.

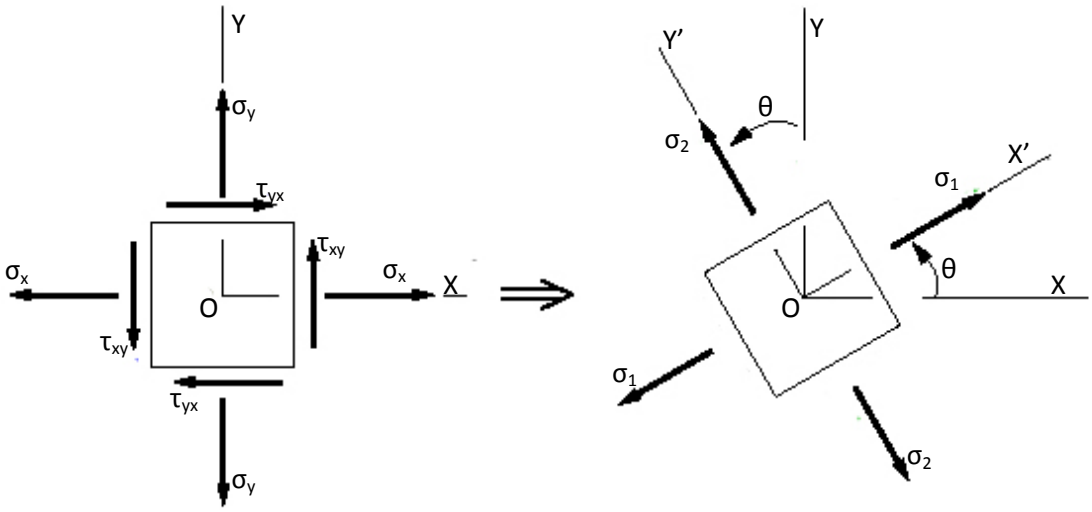

Figure 5: Principle Stress Description.
On the left is a state of stress with stress in both X and Y as well as shear. If the object that the stress is being evaluate is rotated as is shown on the right, then all shear stresses disappear leaving principle stresses.

In engineering mechanics predicating the deformation and failure of a system is often the goal. Several methods exist for predicating the failure of bulk or main body of the system. Two of the most common methods are the Tresca and von Mises yielding criteria. Each of these methods use the principle stresses in comparison to the yield stress. For the Tresca requirement Equation (1) must be meet, while the von Mises criterion follows Equation (2) [6]. In this way the Tresca criteria is more conservative than the von Mises requirement as Tresca follows linear relationships while von Mises follows an elliptical criterion [6].

$$\begin{matrix} |\sigma_1| < \sigma_y \text{ and } |\sigma_2| < \sigma_y \text{ if } \sigma_1 \text{ and} \sigma_2 \text{ have the same sign} \\ |\sigma_1 - \sigma_2| < \sigma_y \text{ if } \sigma_1 \text{ and} \sigma_2 \text{ have diffrent signs} \end{matrix} \quad \textbf{(1)}$$

$$\sigma_1^2 - \sigma_1\sigma_2 + \sigma_2^2 < \sigma_y \quad \textbf{(2)}$$

In this project the objective is to create a crack or the failure of a system. In a failing system with cracks, a local stress value is higher than the bulk material stress (σ_{Bulk}) and the Tresca and von Mises yielding criteria can no longer be used. The reason for local stress

concentrations is that the crack, like a hole in the material, is an imperfection which causes the force to be distributed over less material. Since the force is distributed over less material, this increases the local stress value. In these systems, local stress values (σ) can be determined by calculating the stress concentration factor (K), which is dependent on geometry, and multiplying this by the bulk material stress as shown in Equation (3). To demonstrate the change in stress distribution on a plate with a hole in it, Figure 6 is offered. The idea that local stress values are higher than the bulk due to stress concentrations is one of the driving principles for crack propagation. Locally at the tip of a crack, the stress is much higher than in the bulk of the material. This increased local stress, causes the crack to grow in order to equalize the energy in the system.

$$\sigma = K\sigma_{Bulk} \quad \textbf{(3)}$$

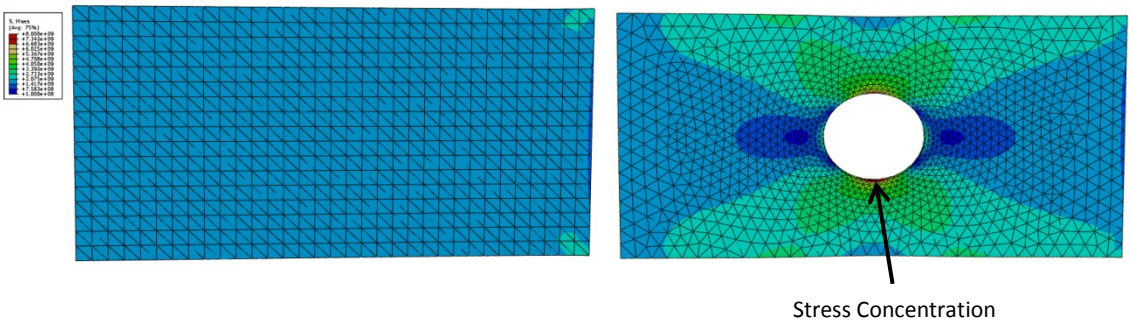

Figure 6: Stress Concentration Example.
The plate on the left is a homogenous, while the plate on the right has a hole causing a stress concentration. The right wall of the plate has a non-translating constraint, while the left wall has a tensile or outwardly directed pressure applied.

1.4 Vibrations

A mechanical vibration is mechanical oscillation of an object about a point of equilibrium. Mechanical vibrations have long been a topic of interest dating back to the discovery of musical instruments such as stringed instruments. Wallis and Sauver both observed the phenomenon of modal shapes in a vibrating string [7]. These modal shapes are shown in Figure 7, and can cause a difference in pitch and tone for an instrument, as discovered by Hooke [8]. When a system, is vibrated at one of its natural frequencies, shown in Figure 7, the system is said to be in resonance. When a system is in resonance then excessive deflections exist in the system as can be seen for each mode in Figure 7.

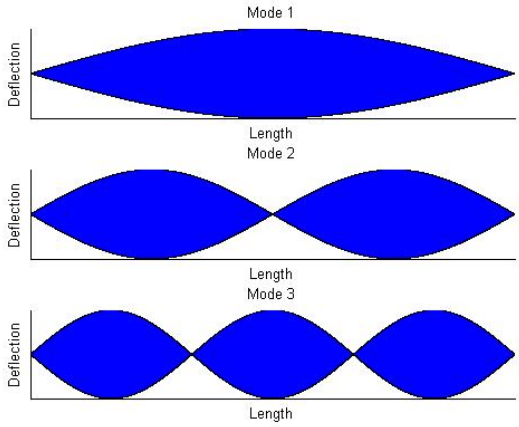

Figure 7: Example Modes for a String.
Shown are the example modes for a string with constant length and tension. As the mode increases the peak deflection does not change but rather the number of points reaching this peak.

In vibrations, it is often convenient to describe a vibration wave packet as the linear super position (or addition) of base vibrations. This concept was first proposed by Bernoulli [9] and is shown in Figure 8. Vibrations can be classified as either random vibration (unpredictable over time) or deterministic (predictable and cyclic). Due to this generalized definition, mechanical vibrations can be used to describe many aspects of life such as hearing (vibration of

the ear drum), breathing or the vibrations of the lungs and even walking can be described by the periodic motion of the arms and legs.

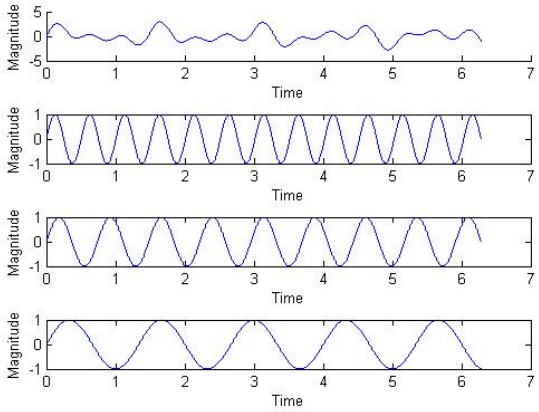

Figure 8: Superposition of Wave Basses.
The top wave packet is the superposition of the bottom three waves. In this way a complex wave can be described as a set of simple waves

In mechanical design it is often important to evaluate the vibrations of a system because they can lead to catastrophic failure of the system. For example in turbines, even the slightest imbalances in the turbine blades, caused by faulty manufacturing or poor design, cause large vibrations in the system causing its failure. Other mechanical systems experiencing regular vibrational forces are centrifugal machines, motors, engines and reciprocating machines and pumps. One of the leading causes of failure of these well balanced systems is fatigue caused by the vibrations within the system.

Further classifications for vibrations include free versus forced vibration. In a free vibration after the initial perturbation (or disturbance) the system is left to vibrate on its own without external forces. A forced vibration on the other hand is when a system is subjected to an external repetitive vibrational force. An example of a free vibration would be the pendulum in a grandfather clock, while a diesel engine would be an example of a forced vibration. Additionally a vibration can be described as undamped or damped. In an undamped system no

energy is lost or dissipated during the oscillation. If the system is free, then the system will vibrate forever. In a damped freely vibrated system, energy is dissipated in the system and will eventually stop vibrating. Quantifying dampening is done with the dampening ratio (ζ) and this is a measure of how quickly energy is dissipated from a system. In this way as the dampening ratio increases, then energy in the system will dissipate more quickly.

CHAPTER 2 LITERATURE REVIEW

2.1 Revision Total Hip Arthroplasty

In an increasingly aging yet active population a larger number of people are electing to get an THA each year, at younger and younger ages. Given that more people are electing to get this surgery and revision rates are estimated at 17.5% over the lifespan of the implant more hip replacements will need to be replaced [2]. Revision total hip arthroplasty (rTHA) can become necessary for a variety of reasons; which include: pain, typically caused by implant instability and loosening, 66% of revisions, infections, 14% of revisions, and stem fractures, 3% of revisions [10-12]. The revision surgery is an invasive process, which requires an expert orthopedic surgeon, long operating times, and high costs; as such rTHA is considered a last resort method of treatment. Revision total hip arthroplasty requires a large amount of preoperative planning to determine the type of Implant Along with the type and amount of implant fixation [10, 13, 14].

Implants themselves have a variety of shapes, sizes and features. Early implants were made primarily of stainless steel L316, whereas now it is more common to use Cobalt-Chromium alloys (ASTM F-75 and ASTM F-76) or titanium alloys (ASTM F-136) [15]. Additionally more than ten major manufacturers provide new implants each year. Variable to the implant design are features such as: a permanent or screw on femoral head, ribbed or non-ribbed, smooth surface or implants with porous coatings. Just a few of these features are shown in Figure 9 [16].

Figure 9: Common Femoral Implants.
Presented here are several of the different types of implants which can be used in THA.

Smooth implants are used in conjunction with polymethyl methacrylate (PMMA) bone cement for fixation, whereas porous coated implants were developed for boney growth to be the fixation mode [14, 17]. For a cemented implant the typical revision surgical plan begins with the removal of the implant from the cement, followed by the removal of the cement mantle from the surrounding bone stock. The removal of the implant is typically done with a trochanteric osteotomy (Figure 10), to gain access to the implant cement interface [10]. A trochanteric osteomtomy is a process where a cut is made into the femur at the greater trochanter, and this portion of the bone is then excised Once access to the implant-cement mantle interface has been gained, a variety of specialized tools are used to free the implant from the cement. These tools include pneumatic cutting tools and osteotomes most of which are specific to the Implant being removed (Figure 11). Once the implant has been separated from the cement mantle, a shaft or slap hammer is used to break the remaining bonds affixing the implant to the bone. At this point the PMMA mantle must be removed from the surrounding host bone so that a new implant can be fitted. The removal of the cement with minimal damage to the bone requires specialized cement removal tools, osteotomes, reverse cutting hooks, drills, taps and chisels [14, 18]. In some cases it becomes necessary to make small windows in the bone and use endoscopic instruments for better visualization of the cement mantle [18].

Once the cement has been removed, the surgery may proceed like a normal total hip replacement surgery, however less bone stock is available for implant fixation.

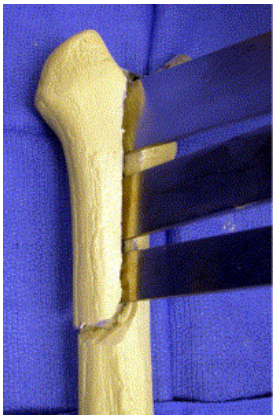

Figure 10: A Trochanteric Osteotomy.
Left trochanteric osteotomy on an extracted femur [19].

Figure 11: Osteotomes.
Osteotomes are tools are used to separate an implant from its connective interface[20].

Cementless or porous coated implants follow a similar protocol for removal as the cemented implants. A trochanteric osteotomy is used to gain access to the bone-implant interface. Next the implant is attempted to be removed with the slap hammer. At this point two scenarios present themselves; (i) instability is found between the implant and bone, or (ii) stability is found [10]. If instability is found disimpaction is continued with the slap hammer. If stability is found effort is then placed into accessing and dividing the bone implant interface. This is done using the same tools used to separate the implant from the cement mantle;

however the tools have been adapted to cut through the metallic implant. This process can lead to cuts and fractures in the host bone, and is continued until the implant is removed [17].

Since current methods for removing the femoral implant from the bone can cause fractures, loss of healthy bone, are invasive and consume large amounts of time and subsequently money, other methods for removing the implants are being developed and tested. Two newer methods include the use of lithotripsy and high energy ultrasonic waves [21, 22]. Lithotripsy is a non-invasive treatment typically used to destroy renal stones, in the urinary tract. It works by applying a highly focused, high intensity acoustic pulse. For cement break up, the acoustic pulse is focused at the cement mantle, and has been shown to reduce the fracture toughness of PMMA by as much as 14% [21]. This allows for both the implant and cement mantle to be extracted more easily. Another method uses high energy ultrasonic waves into the cement mantle. This energy is then absorbed by the PMMA resulting in a temperature increase. This energy is applied to the PMMA until it softens to a dough like state, allowing the removal of the implant with minimal effort [22]. The use of lithotripsy is not commonly used as a preoperative rTHA treatment due to the potential damage that could be caused to the surrounding bone stock. If the shockwaves were misaligned the potential damage to the surrounding healthy bone is high. The use of high energy acoustic waves to heat the PMMA is also not commonly used as it requires expensive specialized equipment, and has not yet been fully tested. As such a need exists for an inexpensive, minimally invasive, easy to use technique and tool for the removal of a femoral implant from cement or bone in rTHA.

Summary

Revision rates for THA are estimated at 17.5% and are required for a variety of reasons including implant instability (or loosening), infections and fractures [2]. Performing an rTHA is a time consuming, costly surgical operation that requires a surgeon with expert skills. While the

implant in the patient may greatly vary in its shape, size, and fixation the process for removing the implant is always similar. The goals are to break the interface between the implant and bone/cement, done with special surgical tools often developed for the specific implant. In most cases a trochanteric osteotomy must be performed where a large section of the femur (near the hip) must first be excised. When the bonding between the implant and bone/cement is mostly broken a slap hammer is used to break the final bonds. Since current methods of removing implants are so invasive and costly, the orthopedic community is constantly looking for and evaluating new methods or improvement to current methods for removing implants that are (i) less invasive, (ii) require less surgical skill and (iii) take less time to perform.

2.2 Vibrations

The objective of the proposed device is to utilize vibrations to aid in the removal of a femoral implant from its surrounding cement mantel; however what frequency to operate at has yet to be determined. The method proposed here is to utilize the implant's natural (or resonate) frequencies. Resonance is the tendency of the system to respond at greater amplitudes when the vibrational frequency matches one of the system's natural frequencies. For example, a child on a playground swing can act as a pendulum. If the child is pushed in time with the natural interval of the swing, the child will go higher and higher each time. In this case, the pushing force is acting at the swing's natural frequency and operating in resonance. If, on the other hand, the pushing force is acting at any other time, the swing will go slower and could even stop; the pushing force is then said to dampen the swing. For this reason, putting an implant into resonance will require the lowest amount of mechanical energy input to generate large forces.

Natural frequencies themselves are dynamic. As the system changes, due to damage, the natural frequency will evolve. This is especially important since resonating a system at its natural frequency can lead to catastrophic damage, caused by the vibrational force building on itself. Just like the example with the swing going higher and higher, the vibrational force will get larger and larger. Depending on the conditions this can lead to disastrous damage; one example of a system being damaged due to vibration at its natural frequency is the Tacoma Narrows Bridge. In November 1940 in Tacoma, Washington, a bridge was being vibrated by aerodynamic forces caused by wind speeds in excess of 40 mph [23]. After 45 minutes of being vibrated in resonance, the amplitude of the vibration had built to such a point that the bridge collapsed. It is this same destructive resonance force that the proposed device will exploit to separate an implant from its surrounding medium.

Determining the natural frequency of the implant, however, is not a simple task. Two basic methods are currently employed; the first is to experimentally determine the system's natural frequencies, and the second method is to calculate the natural frequencies using the finite elements method (FEM). In order to experimentally determine the natural frequencies of a system, an expensive function generator and a very precise accelerometer need to be used. Determining the natural frequencies of a femoral implant in bone has been well researched as a means of determining component loosening of the implant [24]. Typically a function generator delivers a controlled excitation to the implant. The accelerometer would then be mounted somewhere distally of the implant to measure the transmitted vibration, and the natural frequencies are then determined with post processing. Determining the natural frequency using FEM is a more efficient process, however it is highly dependent on boundary conditions as well as the accuracy of digitizing the geometry. Generally, finding the natural frequencies of an object involves digitizing the object through 3D scanning. Applying material properties for bones can be done with the computed tomography (CT) data, and then boundary conditions matching the testing conditions are applied. Taylor et al. explored both the experimental and computational methods for determining natural frequencies of a human femur [25]. Their experiments determined that errors using the computation methods were less than 8% over the first four modes.

Because operating at a system's natural frequency has such a destructive force, it is not commonly modeled to cause damage. However, one well-controlled wave packet that is often modeled to cause damage is found in the form of fatigue testing. In this type of testing, a load varying between a maximum and minimum is applied to a sample at a slow frequency. The frequency used is typically low enough such that complex time dependent effects, such as strain rate, can be disregarded. This frequency is dependent on the mechanical properties of the

material; for bones a frequency of 15*Hz* or lower is typically used. In practice, four-point bending tests are often used for fatigue analysis of a sample. In a four point bending test, a sample is placed on two supporting pins, and then two loading pins provide force as shown in Figure 12. This creates a region of pure bending between the two loading pins.

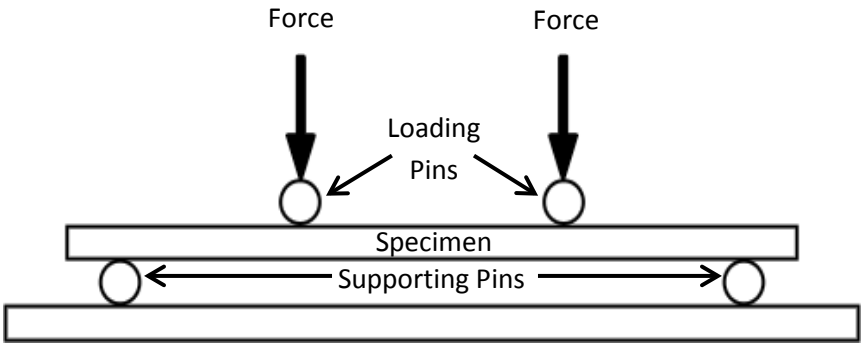

Figure 12: Typically Loading for a Four-Point Bending Test.
Here is the typical loading setup for a four-point bend test.

Four point bending tests are used to analyze the fatigue strength for systems of all sorts. One system that is similar to an implant in a cement mantel is the use of rebar with concrete. In this analogy the rebar acts like the femoral implant, and the cement is analogous to the PMMA. When materials are compounded in such a way (i.e. nonhomogeneously), one serious problem is debonding of the added material from the bulk material matrix (e.g. debonding rebar from cement). Whab et al. performed a fatigue test of cement beams with rebar aligned axial to the beam using a four-point bending test rig [26]. Their tests showed that debonding the rebar from the cement matrix exhibited less resistance than trying to fracture the cement in shear (direction perpendicular to rebar). In other words, their study concludes that the easiest or most probable way for a beam to fail was though debonding of the rebar from the cement, as opposed to shearing, buckling or necking. Another similar study performed by Zhang et al. showed that debonding rates of rebar from cement were highest during the beginning stages of fatigue testing [27]. This was attributed to the initially rough surfaces on the rebar: as the

surface roughness decreased, the friction between the cement and rebar increased causing, debonding to slow.

Fatigue testing of an implant/cement system cannot effectively use a four point bending test because *in-vivo* the forces are not directed in such a manner. Rather, forces are directed compressively into the femoral implant and as such, *in-vitro* simulations must be tailored around this principle. For hip replacements, fatigue fractures in the bone cement mantel are one mechanism for component loosening of the femoral stem. Some of the factors influencing the fatigue life the PMMA include: porosity, residual stresses, and viscoelastic effects. Porosity of bone cement has a well-documented problem of initiating micro-cracks and facilitating their coalescence. Jeffers et al. [28] applied a cyclic load of 3.5 body weight, based on a 70 kg person to a femoral implant, surgically implanted into a cadaveric femur at a rate of 2*Hz*. They found that failure occurred for the system between 300 and 100,000 cycles. After failure occurred, micrographs revealed that fatigue failure of the system originated at the stem/cement interface. Ramos et al. [29] performed a similar study confirming that porosity indeed played a vital role in the fatigue life of the cement mantel. Additionally, they observed that fatigue damage was strongly correlated with cement mantel thickness, where 2 to 3*mm* was considered to be optimal. Finally, in a second study they found that fatigue fractures originated at the stem/cement interface when the cement mantel thickness was less that 5*mm* [30]. Figure 13 shows the cracking at several locations along the implant cement interface. When the cement mantel thickness was above 5*mm*, they observed that fatigue fractures originated at the bone/cement interface.

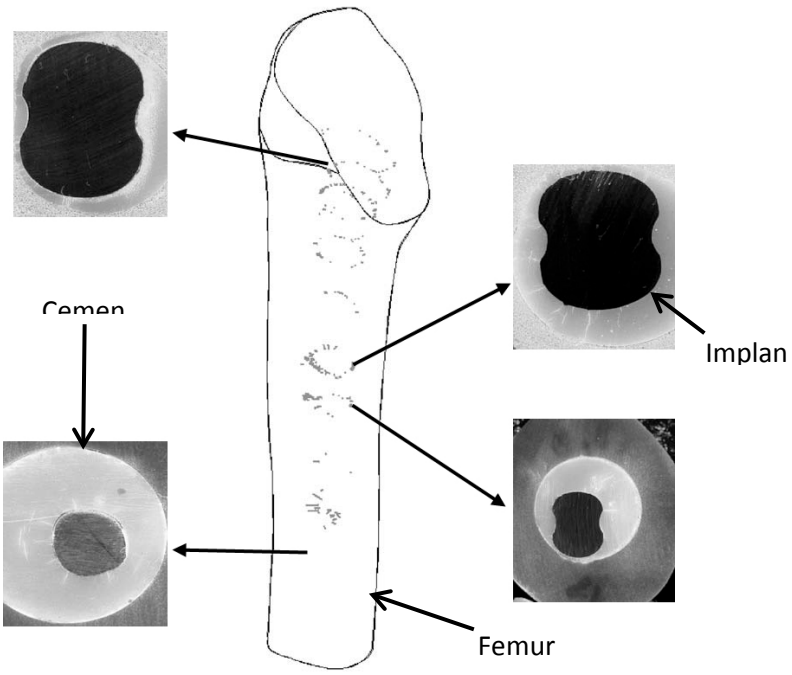

Figure 13: Damage of the Cement Mantel in the Ramos et al. Study.
It can be seen from this study that fatigue cracks initiate at the cement implant interface, and that damage is substantial.

Summary

The principle of this thesis is to vibrate an implant at its mechanical resonance in order to separate the implant from the cement mantel. It has been well documented that putting a system into its mechanical resonance can have catastrophic effects as is seen in the Tacoma Narrows Bridge. The system in this thesis is an implant surrounded in cement, in this scenario the cement can be thought of as a dampener on the implant reducing the effectiveness of the resonance frequency. No literature could be found for placing an implant into its resonance frequency for an extended period of time; however a slow well controlled wave packet has been well studied in the form of fatigue testing. This testing has shown that a system consisting of two mating materials is weakest at the bonding interface, and in hip implant systems the cement is susceptible to cracking at the cement implant interface.

2.3 Finite Elements Method

Finite element (FE) modeling is a numerical method of solving problems in engineering and mathematical physics. Typically this method of solving problems is applied to areas such as structural analysis, fluid flow, mass transport, heat transfer and electromagnetic potential [31]. Finite element modeling is often used to solve problems involving either one or all of the following: complex geometries, complex loading conditions, complex boundary conditions and large number of material properties [32]. In these scenarios it is generally not possible to derive an analytical solution where desired values can be generated for any position using a mathematical expression. These types of solutions are generally the result of solving differential equations, many of which are insolvable due to the complexities of the problem. For this reason, engineering often relies on numerical methods such as FE modeling in order to approximate the analytical solution.

Finite element solutions involve breaking the problem into small elements for which algebraic approximations may be used to solve the system rather than differential equations. In FE modeling, equations are formulated for each “finite element” resulting in solutions at each “node” in the element. To do this, equations for each element are combined allowing for a solution to be generated for each node [32]. For this reason the division of the system into elements must be fine enough to generate accurate results, yet be course enough so that the solving time can be handled by modern day computational power [31]. Typical desired solutions in structural FE modeling include stress and strain distributions, determination of damage accumulation and system resonant frequencies.

The finite element method (FEM) as we know it today began its development in the 1940’s [33], more recently in the 1970’s FEM was used in fields such as bioengineering [34]. Within bioengineering FE modeling is used in a plethora of ways, one of which is to simulate

factors influencing femoral implants inside of a femur. To solve this system all of the parts must first be meshed, where the included parts typically consist of an implant, a cement mantel and a femur. When modeled in 3D many of these models use either an 8 node brick element [35-37] or tetrahedral elements [38, 39]. Advantages of the 8 node brick element is that they tend to give more realistic answers for a courser mesh, however they are difficult to mesh for complex geometries. Tetrahedral elements on the other hand need a finer mesh for accurate results, but are adaptable and can mesh nearly any geometry [40].

One of the critical factors affecting hip implant modeling is how to model the interface between the implant and the cement mantel. Most of the modeling performed evaluates the stress distribution of the implant on the bone caused by normal operating conditions such as walking and running. This means that the load, is applied though the center of the femoral neck resulting in a pushing force [35-38, 41]. In this scenario it is common for researchers to model the implant cement interface as a frictional interface where friction (μ) varies between 0.15 and 0.35 [35, 38, 41]. These models have shown to be very effective when evaluating a pushing force on the femoral neck, however when a pulling force is applied, the model does not perform as well. Rather implant fixation is normally assumed to be perfect and elements are constrained on the two surfaces resulting in zero motion between them [35, 37, 42]. Boundary conditions very from model to model due to geometrical difference, however only proximal half of femur is normally modeled (the half with the implant). With this restriction, the cutoff surface on the femur is normally grounded, such that it is non-translating and non-rotation [35, 36, 38].

It is often advantageous to take such a model, where stress distributions can be solved, and determine the amount of damage to the system from the applied loads. Often engineering stress levels can be compared to bulk material properties to determine if the part or system will fail. These methods such as von Mises and Tresca criterion involve seeing if any state of stress in

the system is higher than the bulk yield stress of the material. These methods, however, fail to account for damage that can accumulate in a material thus increasing local stress values and propagate damage typically in the form of a crack. To model this in FE two methods are commonly used, the cohesive zone model (CZM) and the extended finite elements (XFEM). In the CZM cohesive zone elements are usually elements placed on the surface between bulk element boundaries. Thus crack growth only occurs between bulk elements resulting in a mesh dependent algorithm. In this model the crack direction becomes highly dependent on mesh texture and alignment, and it often requires re-meshing during the solving phase[43]. In lieu of these and other problems associated with CZM the XFEM method was proposed as a mesh independent way of calculating crack growth. XFEM is based on the partition of the unity property, where local enrichment functions are included in the standard FE modeling adding additional degrees of freedom to cracked elements [44]. This however, requires external criteria in order to predict crack growth such as the concept of the stress intensity factor and the maximum principle stress criterion.

The field of fracture mechanics is a relatively new field, when compared to other mechanics of material fields; as such research effort is still being devoted to fracture mechanics theory. As a result many researchers are using custom written algorithms to computationally evaluate fracture mechanics methods. It was not until recently that Abaqus (the FE software package used in this thesis) incorporated XFEM into the standard distribution. The release of Abaqus 6.9 [45] in 2009 marked the introduction of XFEM into Abaqus, and each successive release of Abaqus has made major improvements in the predicative capabilities of the standard XFEM package. Even though the exact solutions from XFEM differ from experimental results, general treads seen in XFEM are also seen in experimental results[44]. For example calculated crack branching in XFEM lacks some of the minor branching that is observed in experimentation

[46]. Major branching and calculated crack speeds in XFEM however are well simulated, similarly calculated major cracking geometry and crack speeds are on the same order of magnitude as experimental results [43].

A newer novel application of FE modeling is to calculate the natural frequencies of the femoral system with an implant. It can be shown that a wide range of natural frequencies can be derived from this system, which indicates the level of fixation for the Implant As mentioned in Section 3.2. As previously stated the accuracy of calculating the natural frequency of an object through FEM can be as high as 95% accurate compared to experimental methods [39]. The model setup for frequency analysis is similar as the processes for evaluating stresses. An implant and femur geometry are first obtained, most often though the use of computational tomography (CT) data. The implant and femur are then segmented and imported into an FE software package and they are both meshed using either brick or tetrahedral elements [39, 42, 47, 48]. The interaction between the implant and the surrounding material is always modeled as either completely bonded [39, 42, 48] or with a frictional model [42, 47]. Typically the system only models the proximal half of the femur, and the section cut is grounded. Material properties are then applied to the model resulting in first mode natural frequencies ranging from 100 to 300*Hz* depending on both the material properties and fixation level of the implant.

Summary

Finite element modeling is a process of breaking a complex problem into finite number of small problems where solutions can be found at each element's nodes. In modeling an implant femur system, it is most common to use a brick or tetrahedral elements. Tetrahedral elements are the easiest to mesh complex geometries; however they require a larger number of elements to accurately model the system. In the implant femur system the interface between the implant and the cement is a very important interaction for accurate modeling. For a compressive model, a friction interaction is typically used between the implant and the cement.

Whereas in a tensile test, a normal force does not exists between an implant and the cement so a friction model cannot work. For this reason a tie constraint is used to simulate perfect fixation between the implant and the cement where no motion of the surfaces exist between the implant cement. To simulate damage accumulation in such a system it is most common to utilize XFEM. This method is new and changing to match the evolving theory behind this method, however general trends shown in XFEM calculations are expected in *in-vitro* testing. Finally using FEM to calculate the natural frequency of a system, such as this, is a common procedure. It has been shown that FE modeling can be has high as 95% accurate for determine natural frequencies.

CHAPTER 3 INTRODUCTION

3.1 Motivation

Revisions for THA are currently estimated at 50,000 per year, but projected to increase to over 100,000 in the next 17 years [2]. These revision surgeries become necessary after the failure of a primary hip replacement surgery were the most common reasons for rTHA include implant loosening, infection, and fracture of the implant. With an increasing number of total hip arthroplastys (THAs) being performed each year, the number of rTHAs being performed has also increased at the same rate; despite improving surgical techniques and decreases in failure rates [10-12]. Performing an rTHA is an arduous task where significant time, effort and surgical skill are devoted to removing the previously implanted device. The long term goal of this project is to provide significant advantages over current surgical procedures, by utilizing an implant's natural frequency to debond the implant from its surrounding bone cement mantel. To remove the implant in an easier, less skilled manner, it is proposed to put the implant into its mechanical resonance, in other words vibrate the implant at its natural frequency. In application mechanical resonance is often avoided as it can cause catastrophic failure [7], but it is proposed here to safely cause the failure of the PMMA cement mantel surrounding the implant allowing for the implant's extraction.

The current study aims at exploring the relationship between an implant's bonding and operating at its resonate frequency with both *in-silico* and *in-vitro* testing. *In-silico* modeling is offered as a proof of concept and is used to determine implant's natural frequency modes, as well as determine the level of failure of the surround cement mantel. Since FE modeling has been shown to accurately determine the natural frequency of objects, up to 95% accurate [39], this will be the method used to determine an implant's natural frequencies. Additionally once the natural frequencies are determined, an implant will be digitally embedded in a PMMA cement mantel. The implant will be digitally resonated by a vibrational force, and the critical

interface between the PMMA and implant will be modeled as a perfectly bonded (tie constraint) interface. Failure of the cement mantel will be modeled with XFEM techniques, which will show the trends of the predicated cracking in the cement mantel. *In-vitro* testing focuses on the design and calibration of a prototype as well as a experimental validation of the *in-silico* finding. Given the goal of this project three main objectives are proposed in designing a device utilizing vibrations to remove a femoral implant.

3.2 Objectives

1. Characterize implant design parameters, which affect the natural frequencies of an implant using computational modeling.
2. Demonstrate cement crack propagation due to a low amplitude mechanical vibration for an implant-cement computational model.
3. Design a prototype device that can (i) integrate easily with current operating room devices, and (ii) transfer vibrational energy to a wide variety of commercially available implants.

In the remaining chapters of this thesis, Chapter 4 describes *in-silico* modeling. In this chapter implant design parameters affecting natural frequencies are first explored. Next a computational model is developed to simulate vibrating an implant at its natural frequency. Finally, this chapter concludes with utilizing XFEM techniques to demonstrate crack propagation in cement due to natural frequency vibrations. In Chapter 5 *in-vitro* testing and device conceptualization is offered. First, the prototype device design and modifications are discussed. Next, device calibration is explored, and finally this chapter will conclude with *in-vitro* testing of the prototyped device. Finally, this thesis will finish with a summary, conclusions and study limitations and future work in Chapter 6.

CHAPTER 4 IN-SILICO TESTING

4.0 Introduction

The end goal of this project is to build a device which utilizes the natural frequencies of an implant in order to separate that implant from the surrounding cement mantel. Critical to the development of such a device is to characterize implant design parameters affecting natural frequency, and show that crack propagation can be initiated when an implant is subjected to resonance frequency. In this chapter, *in-silico* testing is used to determine the natural frequency of various implants, and demonstrate that resonance can be used to cause cracking in PMMA. As such *In-silico* testing can be divided into three main sections: (i) determination of device operating range, (ii) modeling of an implant cement mantel system undergoing vibrational loading, and (iii) determination of crack propagation in the cement mantel caused by a vibrational load applied to the femoral neck of the implant. Each of these topics is explored in detail in the following chapters. Section 4.1 discusses the determination of the natural frequency in terms of implants geometric factors, boundary conditions (or fixation levels) and varying material properties. Section 4.2 investigates a modeling technique to simulate putting an implant into mechanical resonance with a vibrational force for an implant-cement mantel system. In this system the vibrational force is modeled as a dynamic load acting radially on the femoral neck, and the implant cement interface is modeled as perfectly bonded. Finally, Section 4.3 uses the system developed in Section 4.2 to determine the ability to initialize and propagate cracks in the cement mantel.

4.1 Natural Frequency Calculation

4.1.1 Introduction

In order to computationally evaluate the effectiveness of a vibrational force in the aid of removing a femoral implant, several implant designs need to be analyzed. As previously discussed, in the system being modeled, the implants are to be put in resonance with a vibrational force so as to increase the mechanical efficiency of the device. The range of natural frequencies determined in this section will be used for the design of the device. Not only is it important to know the natural frequency range for device design, but it is also important to know the exact natural frequency for an implant, as this will decrease the effective dampening of the system. This is the same concept used to minimize the effective impedance of the inductor by using an AC current at the inductors natural frequency. Offered below is a method for digitizing implants, as well as calculating an implant's natural frequencies. Since the natural frequencies will be affected by geometry, boundary conditions (or fixation levels), as well as material properties, each of these properties are analyzed separately so as to quantify the effects of each. The end goal of this study is to provide predictions of the expected range of natural frequencies for implants, as well as to quantify effects of material properties on the natural frequencies.

4.1.2 Methods

Ten femoral implants were digitized using a Konica Minolta vivid 910 non-contact 3D digitizer [49], resulting in 3D surfaces at differing angles. All implant surfaces were then combined using the automatic best fit alignment tool in Geomagic Studio 12.0 [50]. Once all surfaces were aligned, the 3D volume representation of the implant was created. Implants were then imported into Abaqus 6.10-EF [51], where they were meshed using tetrahedral elements (C3D10). To verify that results were independent of the applied mesh, a mesh refinement study was performed with multiple seed sizes (10*mm*, 5*mm*, 2*mm* and 1*mm*), while calculating the

implant's natural frequencies with homogeneous material properties. The properties required for natural frequency calculation include modulus of elasticity (E), density (ρ) and Poisson's ratio (ν). After the mesh refinement study was concluded the material properties of the implant were varied so as to isolate the effects of geometry versus material properties on the natural frequencies of the implants. These properties were varied as shown in Table 1 and represented an expected range for implant grade materials [15].

Table 1: Properties Varied in the Natural Frequency FE Modeling

Property	Symbol	Values	Units
Elastic Modulus	E	116, 160, 225, 300	Gpa
Density	ρ	2000, 4500, 6900, 8000	kg/m^3
Poison's Ratio	ν	0.273, 0.300, 0.340	-
Seed size	-	10, 5, 2 ,1	mm

Three boundary conditions were studied to determine the range of natural frequencies for different implant fixation levels. The boundary conditions were non-translating, non-rotating conditions on (i) the full length of the implant, (ii) the first two-thirds of the implant and (iii) the first one-third of the distal end of the implant. These boundary conditions (Figure 14) were used to simulate fixation levels for the implant seen clinically at the time of revision surgery [48]. The full length boundary condition would represent removal of a fully fixed implant due to unexplained pain. The one-third boundary condition was used to emulate a poorly bonded implant, which could be separated with a slap hammer during the revision surgery. Finally, the two-thirds boundary condition was used show the progression of the natural frequency as a function of the boundary condition and represents a failed fixation due to loosening at the time of surgery. To calculate the natural frequency of the given setup, a linear perturbation step was used in Abaqus [51] and set to find the first ten natural frequency modes. Default solution settings were used including a 0.5% residual convergence requirement.

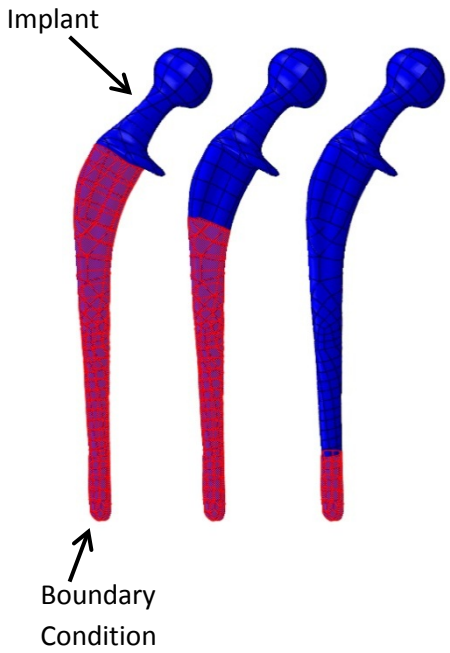

Figure 14: Natural Frequency Determination Boundary Conditions.
Boundary conditions applied to implants to determine natural frequency range. Red area represents surface where boundary conditions have been applied.

Results for all implants were obtained, however only results for two representative implants will be presented. Here in, these implants are referenced as Implant A and Implant B, and are shown in Figure 15. Implant A is the largest implant while Implant B is the smallest, providing the range of results expected for all implants.

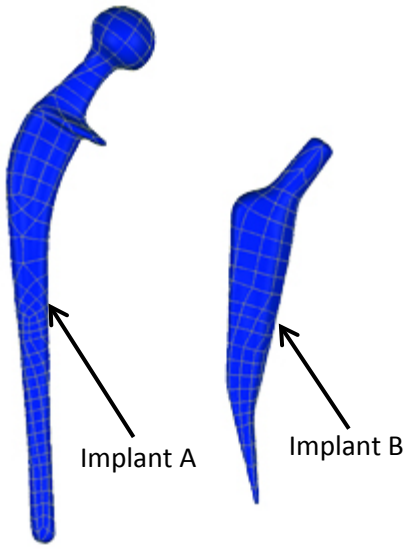

Figure 15: Implants Used in Varying Material Properties Studies.
Left Implant A, right Implant B.

4.1.3 Results

Results for each implant can be broken into three components, (i) mesh independence, (ii) material property dependence and (iii) boundary conditions dependence. For mesh independence, Poisson's ratio, modulus of elasticity, and density were held constant while the seed size was varied to 10, 5, 2 and 1*mm*. For each implant the variation in seed size results in a different number of elements, however if convergence is adequate for all implants for the same seed size, then a consistent seed size could be used for all further modeling. The results from evaluating the first mode for the fully constrained boundary condition for Implants A and B are shown in Figures 16 and 17. An asymptotic relationship exists between the seed size natural frequency and was determined that a seed size of 2*mm* provided a sufficient mesh. This is attributed to an observation of less than 0.2% change in natural frequency for a change in seed size from 2*mm* to 1*mm*. Data for all three modes, for Implant A and B are shown in Appendix A, Tables 4 and 5. Since mesh independence has been established with a seed size of 2*mm* for all implants, further results will be presented only for models with a 2*mm* seed size.

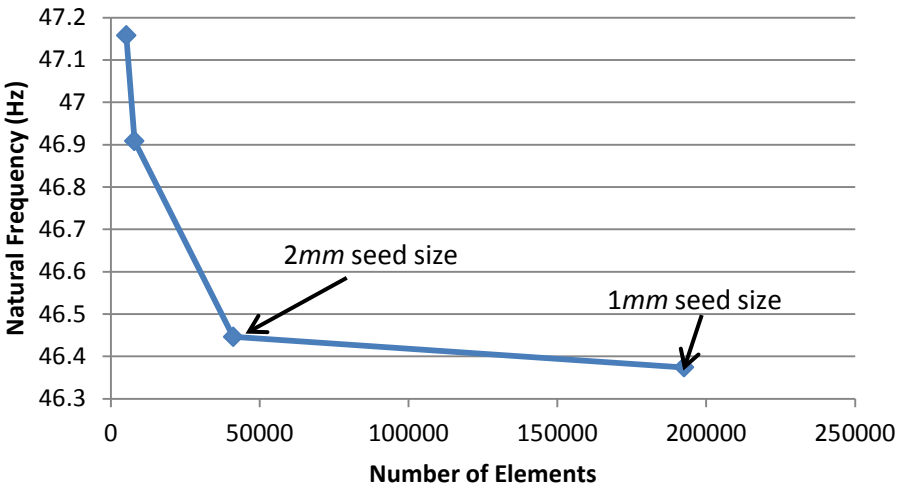

Figure 16: Implant A's Mesh Refinement Study Results.
Results of the mesh refinement study for Implant A. Asymptotic behavior is reached by a seed size of 2*mm*.

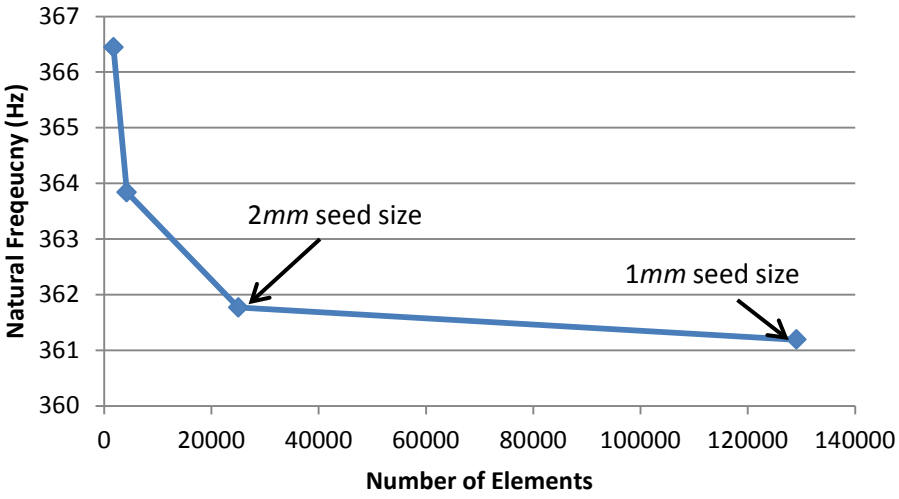

Figure 17: Implant B's Mesh Refinement Study Results.
Results of the mesh refinement study for Implant A. Asymptotic behavior is reached by a seed size of 2*mm*.

The results from the first material property dependence study (Figures 18 and 19 and tabulated in Tables 6 and 7 located in Appendix A) analyze the natural frequency due to a change in density while boundary conditions, modulus of elasticity and Poisson's ratio are held constant. From these results it can be seen that as the density increases, the natural frequency decreases. If the data for each boundary condition is normalized to the first point

(E=2000kg/m^3) then Equation (4) can be used to calculate the effects from changing the material density.

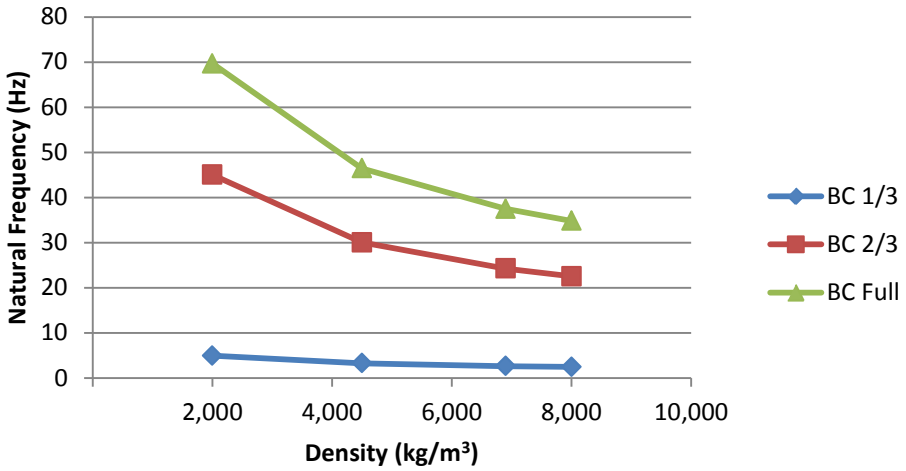

Figure 18: Density Effects on Implant A.
Presented here are the effects of density on the first mode natural frequency for Implant A. It can be seen that as density increases the natural frequency decreases.

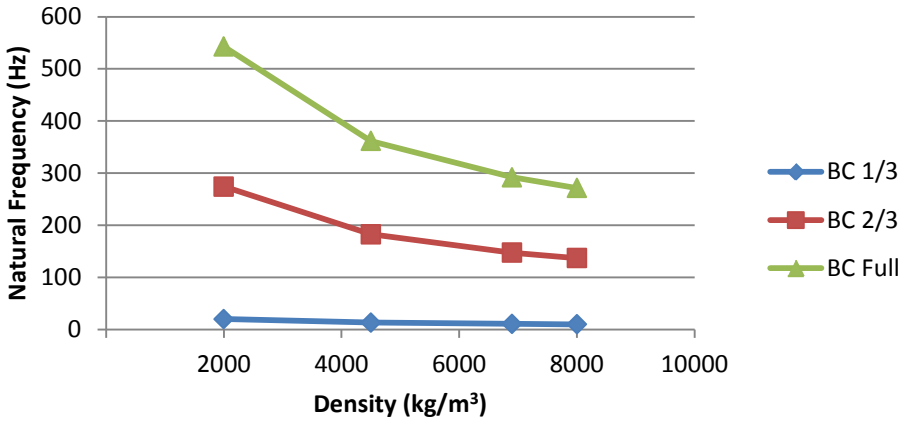

Figure 19: Density Effects on Implant B.
Presented here are the effects of density on the first mode natural frequency for Implant B. It can be seen that as density increases the natural frequency decreases.

$$f = f_o^{\rho}(3.755 - 0.364\ln|\rho|) \quad \textbf{(4)}$$

Here f_o^{ρ} is the natural frequency for the desired mode and boundary condition with a density of 2000kg/m^3. Evaluating the results from the second material property dependence

study (Figures 20 and 21 and tabulated in Tables 8 and 9 located in Appendix A), it can be seen that as modulus of elasticity increases, then so too does the natural frequency. In this study, the modulus of elasticity was varied, while boundary conditions, Poisson's ratio and density were held constant. The relationship between modulus of elasticity and natural frequency can be described by Equation (5) if the data is normalized to any data point.

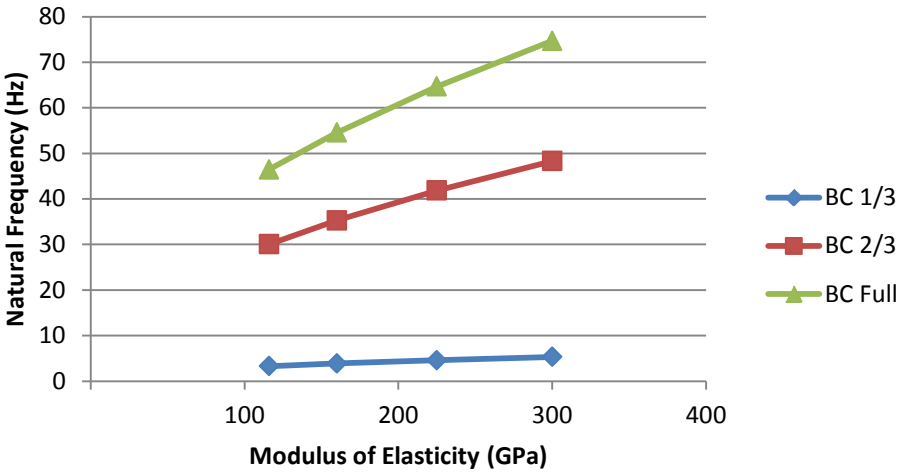

Figure 20: Modulus of Elasticity Effects on Implant A.
Presented here are the effects of the modulus of elasticity on the first mode natural frequency for Implant A. It can be seen that as density increases the natural frequency decreases.

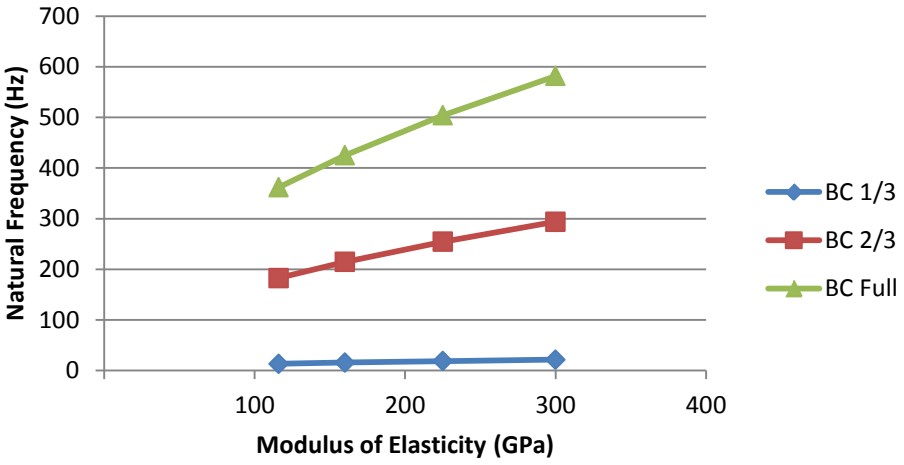

Figure 21: Modulus of Elasticity Effects on Implant B.
Presented here are the effects of the modulus of elasticity on the first mode natural frequency for Implant B. It can be seen that as density increases the natural frequency decreases.

$$f = f_o^E(0.0928E^{0.5}) \quad \textbf{(5)}$$

Here f_o^E is the natural frequency for the desired mode and boundary condition with a modulus of elasticity of 116*GPa*.

An exact equation for the effects of poisons ratio does not exist, however general trends may still be seen; as Poison's ratio increases, then the natural frequency also increases for any mode. These effects however, are negligible as varying between the extreme values in Poisson's ratio (from v=0.27 to v=0.34) resulted in less than 1.5% change in natural frequencies.

Lastly, boundary condition effects can be evaluated by evaluating the trends from all the previous studies. The general trend seen is that as the implant becomes less constrained, moving from the full to the one-third boundary condition, the natural frequency decreases.

4.1.4 Discussion:

As was previously stated, mesh independence was established with a seed size of 2*mm*. This was accredited to a less than 0.2% decrease in in natural frequency for an increase in elements of over 350%. Material property effects can be modeled by Equation (4) for density and by Equation (5) for modulus of elasticity. While equations for Poisson's ratio effects were not established, these effects were negligible as an extreme variance in Poisson's ratio resulted in less than 1.5% change in natural frequencies. Lastly, boundary condition effects were described such that a more constrained or well fixated implant, resulted in higher natural frequencies.

From the data it can be shown that for all the geometry's present in this study, the first natural frequency mode corresponds to an anterior-posterior motion, the second mode correlates to a medial-lateral motion, and finally the third mode equates to a torsional motion

on the transverse plane. For example, the first three natural frequencies are shown in Figure 22 for Implant A.

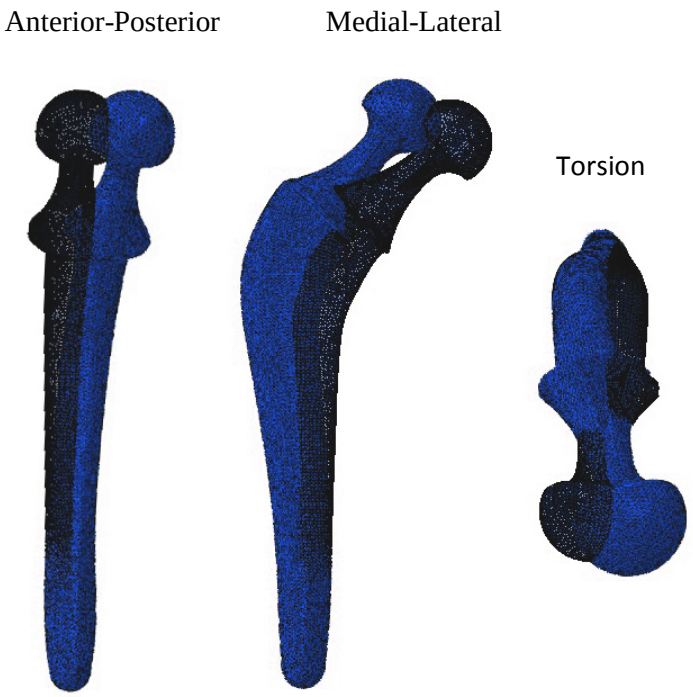

Figure 22: Natural Frequency Mode Deformation Motion.
Motion for each mode given the one-third constrained boundary condition, blue is the deformed state, black outline is the original shape. Deformation has been magnified by 15 to clearly show motion. (Left) Anterior-posterior motion from the first mode, (middle) medial lateral motion from the second mode, (right) torsional motion on the axial plane from the third mode.

Next using Equations (4) and (5) to evaluate the range of frequencies to be expected from four common material implants, stainless steel, cobalt chrome alloys, titanium alloys, material properties tabulated in Table 2 [15, 52], an expected range of natural frequencies can be derived. Looking only at the fully constrained boundary condition Figure 23 shows the expected range for each of the first three natural frequency modes. Only the fully constrained boundary condition is shown, as less constrained boundary conditions will results in similar trends with lower natural frequencies.

Table 2: Material Properties for Implant Grade Materials

Material	ASTM Number	Modulus of Elasticty (Gpa)	Density (kg/m^3)
Stainless Steel	F138	190	8000
Co-Cr-Mo Alloys	F75	300	8300
Ti-6Al-4V	F67	116	4500
Ni45Ti	-	60	6400

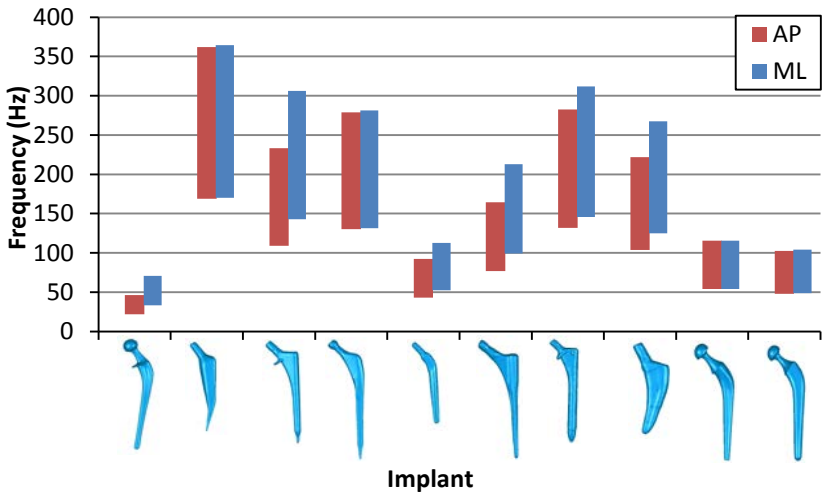

Figure 23: Material Property Frequency Range.
Expected range of natural frequency's for each implant's fully constrained boundary condition given four different materials.

From Figure 23 it can be seen that implants with similar sizes have similar expected ranges in natural frequencies. Since implants typically have similar shapes, similar natural frequency ranges are to be expected, size of the implant has a higher impact on the natural frequency. The general trend is that the smaller the implant the larger the natural frequency. This is similar to a plucked guitar string, the smaller the string that is plucked, the higher the produced note.

4.5.1 Conclusions:

The goal of this study is to first provide an expected range of frequencies that a device would need to operate in. A second goal was to provide predictions on the expected range of natural frequencies of implants and to quantify the effects of material properties. From the

data, an expected operating range for a device would be between 0 and 400*Hz.* This study also shows that if an initial FE model is performed then the effects from material properties can be predicted with equations. Furthermore implants which have a similar size have a similar range of calculated natural frequencies allowing for the predication of natural frequencies. Boundary conditions were also shown to play an important factor in the determination of natural frequency, here a less constrained boundary condition resulted in lower natural frequency. Finally this study concludes that each implant's first three natural frequency modes correspond to an anatomical movement where the first mode corresponds to an anterior-posterior movement, the second mode correlates to a medial-lateral motion, and the third mode equates to a torsional rotation of the transverse plane.

4.2 Dynamic Loading System Response

4.2.1 Introduction

After calculating the natural frequency range of the implants, the next step in the project is to create an accurate dynamic model of the system. In this context a dynamic model is a model where dynamic or time varying loads are applied. Here a vibrational load will be applied to the implant; however the implant is no longer the focus of the study. Rather the cement mantel is the focus, where the end goal of the project is to cause failure of the cement in a clinically relevant manner. As a next step in the modeling of the structural integrity of the cement mantel with a vibrational load, the implant is digitally inserted into a cement mantel. The implant and cement mantel are assumed to be perfectly bonded, and the implant is vibrated with a time varying rotational load. An evaluation of the stresses observed by both the implant and the cement mantel are offered. As a validation of the model, a thought experiment is offered evaluating the time response of the implant to the time varying load applied.

4.2.2 Methods

Implant B was chosen to be the primary focus for this study as its natural frequency range makes it optimal for experimental validation as will be discussed later. It was determined if this implant were affixed in a middle area (Figure 24), the natural frequency would be experimentally optimized. Not only does this middle region provide an experimentally relevant natural frequency, the middle region on the implant has porous coating providing optimal bonding of the implant and cement, representing the most clinically challenging bond to break. After this boundary condition was chosen the methods previously described were first performed to determine the natural frequency modes of the implant with this boundary condition. The implant was given material properties matching the implants composition of Ti-6Al-4V (ρ=4430kg/m^3, E=116GPa and ν=0.342) [15, 52].

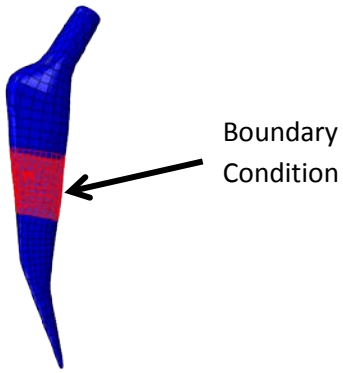

Figure 24: Dynamic Study Natural Frequency Boundary Condition.
Fixed boundary condition used to calculate the implants natural frequency modes.

In clinical applications, the PMMA mantel is between 2 to 5*mm* thick [29, 30]; as such the block that the implant is digitally inserted into must match this condition. To do this, a cement block measuring 25x28x25*mm* was created using Solidworks 2010 [53]. The implant was then aligned in the cement block so that the edges of the implant were between 2 to 5*mm* from the edges of the block before a geometric subtraction of the implant from the block was performed using Geomagic [50]. Both parts were then imported into Abaqus 6.12.1 [54] where they were both meshed with a seed size of 2*mm* (Figure 25). Material properties were applied to both the implant (Ti-6AL-4V, ρ=4430kg/m^3, E=116*GPa* and ν=0.342)[15, 52] and the PMMA mantel (ρ=1190kg/m^3, E=2*GPa,* ν=0.35) [55]. A tie constraint was then used between the two interacting surfaces of the cement mantel and the implant [35, 37, 42]. As such the two surfaces displace the same amount, simulating perfect fixation between the implant and the cement mantel.

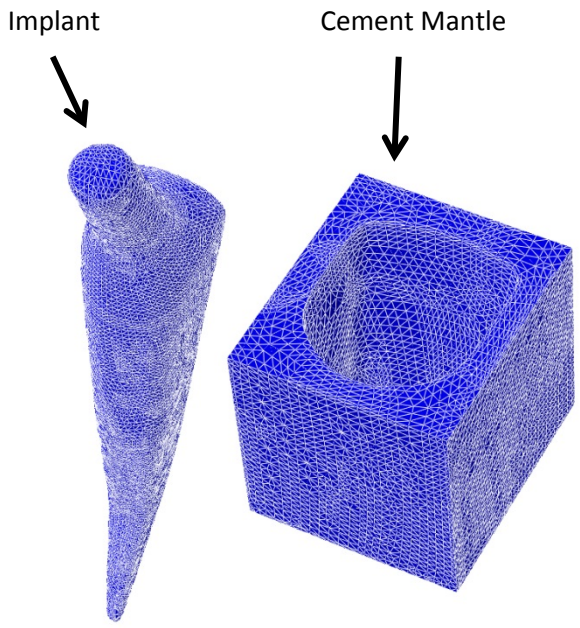

Figure 25: Implant and Cement Mantel Mesh.
Here a mesh has been applied to the implant and cement block using a seed size is 2*mm*.

A "vibrating" load was simulating using a cyclical dynamic load applied to the femoral neck of the implant. The magnitude of this load, 50*lbs*, was calculated based on a 60*g* mass spinning at the first natural frequency mode 180*Hz* of the implant, assuming a radius of 4*mm*. The loading was applied to a set of nodes on the implants femoral neck (Figure 26) such that each node only carries a small portion of the load, preventing any inaccurate distortions caused by point loading. A coordinate system using three nodes on the top surface of the femoral neck was created for the vibrational load, this coordinate system had z pointing axially to the femoral neck, and x and y parallel to the top surface. The vibrational load was applied to the x direction using a cosine function, and a sine function was used for the y direction. As such no axial shear force would be experienced by the implant. Furthermore the system was set up such that when the femoral neck deforms the secondary coordinate system follows these movements and subsequently the loading does as well. This was designed to simulate a spinning weight which can only act radially onto the implant, as will be further discussed in later sections. The cement

block was then given a fully constrained boundary condition on the anterior and posterior sides (highlighted in red in Figure 26). To solve this system a dynamic implicit step was created where the maximum time increment was set to one-tenth of the natural frequency being simulated. Finally the total time for the step was set to be no more than ten revolutions of the load.

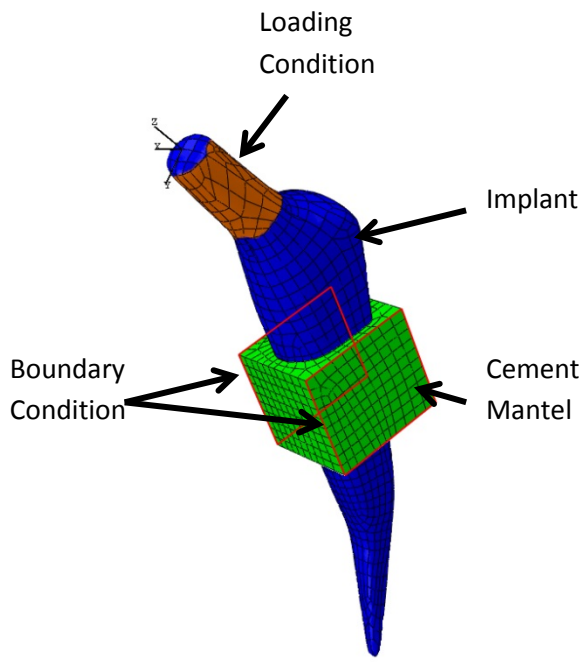

Figure 26: Dynamic Study Boundary and Loading Conditions.
Shown here are the boundary and loading conditions used for the dynamic study. Blue is the implant, and green is the PMMA block. The red outline marks the surfaces where a fixed boundary condition is applied on the cement mantel. Orange is where the loading conditions have been placed on the implants femoral neck.

4.2.3 Results

After ten iterations a pattern immerged on the stress distribution and subsequently deformation of both the implant and the cement mantle. As expected the implant deformed in the general shape of a circle as the force circled around the femoral head. The calculated results from the second vibration divided into ten increments are shown in Figure 27. Calculated stresses fall between 80*MPa* and -97*MPa*, where stresses are focused mainly around the femoral neck and the implant-PMMA interface. An additional observation of the deformation as

a function of time is that the implant exhibits a decaying “shaking” motion on top of the expected circular motion; this will be further explored in the discussion. What is noted is that the shaking happens at a much higher rate than the applied vibrational force and that it is only observed in the anterior-posterior direction.

Evaluating only the stresses translated to the PMMA block, stresses never exceed 15*MPa*. Peak stresses are only experienced on the anterior and posterior sides of the cement mantel, the same sides as the boundary conditions. On the medial side, peak stresses do not exceed 5*MPa*, whereas peak stresses do not exceed 3*MPa* on the lateral side.

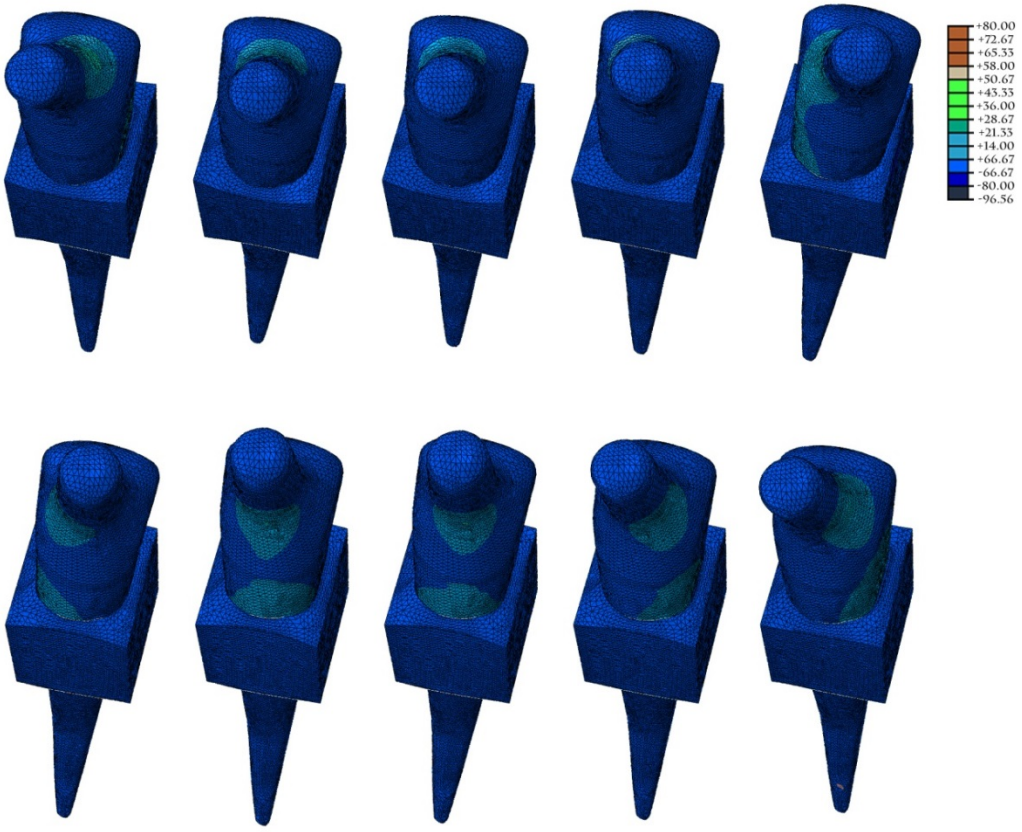

Figure 27: Dynamic Study Results.
Calculated stress applied on the deformed shape of the implant PMMA block system. Shown here is one cyclic vibrational force divided into 10 evenly spaced intervals. Deformation has been multiplied by a factor of 100 to clearly show the deformation trends as a function of time.

4.2.4 Discussion

As can be seen in Figure 27 calculated stress rotates around the femoral neck of the implant. This is an expected reaction as the vibrational force acting on the implant is rotating around the femoral neck at the same rate as the calculated stress is rotating. As previously mentioned the implant experiences a shaking force within the confounds of the applied vibrational force. The observed force declines as a function of time, so it is believed to be a decaying deformation. This deformation can be thought of as an overshoot of the deformation on the femoral neck, like a weight on a spring. At first the implant deforms in the local x direction (anterior-posterior) and deforms too much, as the implant comes back to the steady state position it comes back too far in the x direction since the axial force has rotated from this direction. This is only observed in the x direction as this is the direction with which the vibrational force is first applied. As the implant continues to deform due to the vibrational force, this overshoot settles down and after several loading cycles deformation falls into a near perfect circle. This 2D deformation trend is best described by Equation (6) and is graphed in Figure 28.

$$x = r\cos\big(\theta(t)\big) + r_\alpha \cos\big(\theta_\alpha \cdot \theta(t)\big)e^{(-t/\alpha)}$$
$$y = r\sin(\theta) \qquad \textbf{(6)}$$

Here r is the steady state radius that the implant deforms to as a function of time, r_α is a decaying radius that the implant deforms to. Time is represented with t, while θ_α is a scalar to describe the frequency of overshoot felt by the implant per revolution of the vibrational force. Lastly α is the dampening constant felt by the decaying radius.

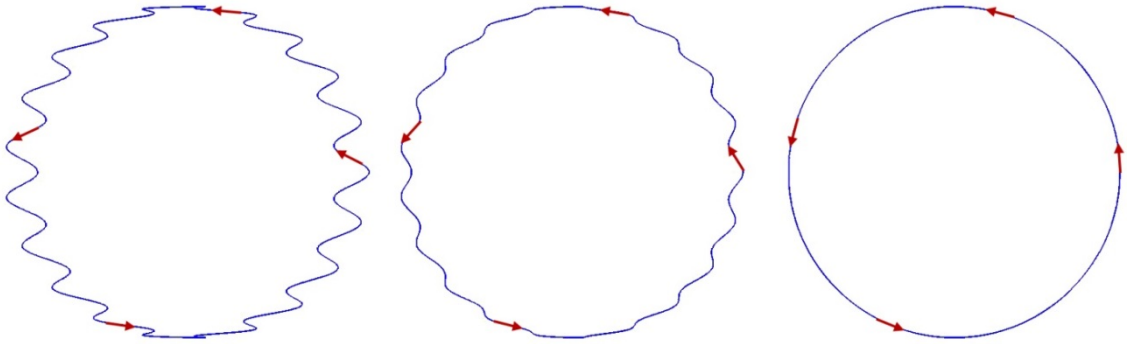

Figure 28: Deformed Path of Femoral Neck.
Displayed here is the deformation path of the femoral neck in 2D as dictated by Equation (6). Changes from left to right represents the decay in shaking as a function of time; $\boldsymbol{\theta_\alpha = 10}$, $\boldsymbol{r/r_\alpha = 10}$, $\boldsymbol{\alpha = 1}$, t=0,1,100. Blue represents the path of motion; red arrows represent the direction of motion.

To put these stresses into context, the maximum principal stress allowed for PMMA is 20*GPa* [55]. So the stresses felt by the cement are 4000 times smaller than the max stress allowed by the PMMA. Additionally the forces felt by the femur performing daily activities like running and walking are higher, forces are estimated at 3*kN* resulting in stresses as high as 30*MPa* in femoral necks[41]. As such in order to have cracks grow in the cement mantel, cracks will first have to be initiated by an external tool.

4.2.5 Conclusions

From this study it can be concluded that initial deformation from the vibration is larger than a steady state condition, despite operating at or near the natural frequency of the implant. This can be thought of as a system similar to a mass on a spring moving in two directions rather than one. The deformation of the implant can be described in 2D as an aggregate circular motion with the addition of a time decaying sine term in the direction of the initial vibrational load. The additional decaying deformation operates at a frequency higher than the vibrational load, however only a general shape has been described, values for the terms in Equation (6) have not been determined. Additionally the PMMA cement mantel can be thought of as a

dampener. This is why a steady state response is reached by the implant while operating at the implants natural frequency, as opposed to diverging deformations.

While exact mathematical models have not been established for the deformation of the implant/ cement mantel system, the general trends are to be expected. Peak stress values in the cement mantel do not exceed 15*MPa*, which occurs on the anterior and posterior sides of the mantel. On the medial and lateral end of the cement mantel, stresses do not exceed 5*MPa* and 3*MPa* respectively. For these reasons it can be concluded that the current system accurately portrays the aggregate trends expected of such a system. Additionally since calculated values of stress fall below the maximum critical stress for bone [56], any device operating at this level should be safe for clinical use.

4.3 Crack Propagation

4.3.1 Introduction

After successfully modeling the dynamic response of the implant-cement mantel interface, the next step was to simulate if and how the cement mantel would fail. To do this the same model as described in Section 4.2 is used, however XFEM is used to model crack propagation. To determine the effectiveness of this new implant removal method, the effects of crack initiation and propagation will be studied in this section. As discussed in the literature review, XFEM provides general trends to be observed in the model rather than exact cracking. So trends found in the models discussed in this section should provide similar trends as those seen during *in-vitro* testing. This section demonstrates that low load mechanical vibrations can propagate cracks in the cement mantel as this is an objective of this thesis; however these crack must be externally nucleated.

4.3.2 Methods

The model as discussed in Section 4.2 has been modified to incorporate crack propagation calculations. This mean that the Implant and cement mantel are still assumed to be perfectly connected, the same loading is applied to the femoral neck in the radial direction, and the anterior/posterior sides of the cement mantel are fully constrained. Both the implant and cement block were meshed with a seed size of 2*mm*, however linear tetrahedral elements (C3D4) elements are used for the cement and implant, as XFEM is only able to operate on linear elements [40]. To evaluate the effectiveness of this technique as a means of removing a femoral implant the cement material properties have been modified to include crack propagation properties (ρ=1190kg/m^3, E=2*GPa,* ν=0.35, σ_1=20*GPa,* K_{1C}=1.17$MPa\sqrt{m}$) [55]. Since expected stress levels in the PMMA are 15*MPa* the model is first completed without initializing a crack. This model was used to verify that (i) crack propagation will not occur when not predicated, and (ii) that an external source is required to initialize the crack, such as a surgeon's device. After

this first initial model was performed cracks were initialized in different locations, to simulate surgically initialized cracks. Cracks are initialized to either the anterior, posterior, medial or lateral sides and are either parallel or perpendicular to the surface of the implant. The cracks are initiated as a plane in the cement block that is 3.5*mm* wide and up to 1*mm* deep. Two of the initiated crack locations as well as the initial and boundary conditions are shown in Figure 29. Futhermore it is hypothosized that reaching mechanical resonance will optimize the process by decreasing the dampening effects of the cement mantel. To verify this assumption, models were also run at half, and quarter first mode resonance freqeucnies or 90*Hz* and 45*Hz* respectivly, using the same crack location and boundary/loading conditions.

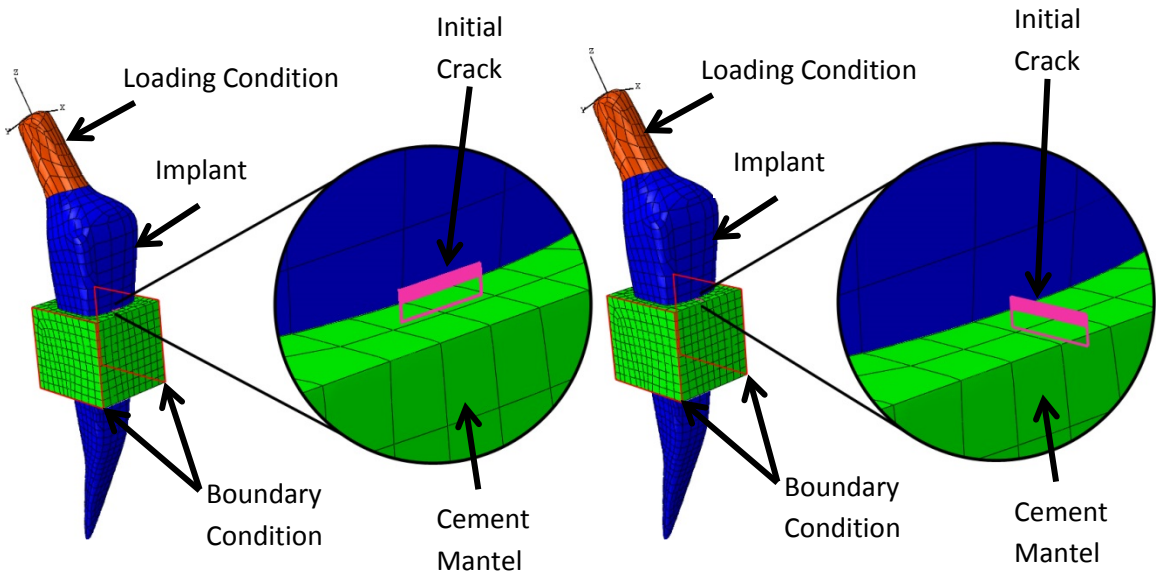

Figure 29: Boundary and Loading Conditions for the XFEM Study.
The implant is blue and the cement mantel is green. Orange is where the vibrational loading has been applied, and the red highlighted surfaces are where the boundary condition has been applied. The pink region is the initial crack. Left: The crack is parallel to the surface of the implant. Right: the crack is perpendicular to the surface of the implant.

A dynamic implicit step is still used to calculate the reactions of the implant and cement to the vibration perturbation. However since Abaqus [54] is now attempting to model a failing model, the standard convergence techniques cannot be used [40]. First off the maximum number of allowed calculated steps has been increased to one million, next the maximum

number of failed attempts to calculate a given time increase has been increased to 100. This means that if the calculation fails, then the increase in time from the last to the current step is allowed to decrease (up to 100 times) before the calculations are aborted. Finally the solution controls have been modified to let Abaqus [54] know that it is trying to solve a discontinuous or failing system [40]. As such when the system fails to meet the typical convergence patterns the program will not abort.

4.3.3 Results

The first model performed was the dynamic model from Section 4.2 with XFEM. As predicted from Section 4.2, no cracking was observed (Figure 30) as stress levels are not large enough to nucleate a crack. Cracked elements in this figure would be displayed as green, while the surface cracks would be outlined in black. To improve the visibility of the cement mantel, the implant has been removed from the view.

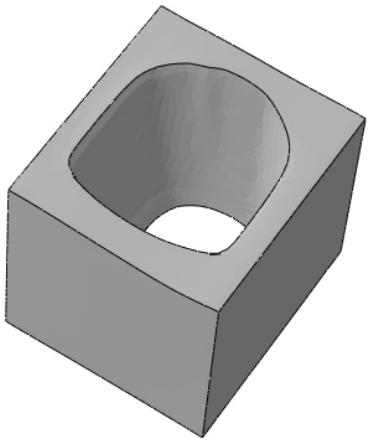

Figure 30: Crack Propagation without Crack Initiation.
Crack propagation for the implant cement mantel system when a crack has not first been initialized.

Next cracks were initialized in the cement mantel, and crack propagation evaluated as a function of both location and orientation of the initialized crack. When a crack was initiated and an implant is vibrated at its natural frequency (200*Hz*), cracking quickly propagates though the

cement mantel. As can be seen in Figure 31 cracking is able to start at one side of the cement mantel and travel throughout most of the implant. In Figure 31, all areas marked with green represent areas that have cracking in them. Cracking has been divided into ten segments in which make up 10% of a full vibrational cycle. In this figure, the crack has been initiated on the lateral end of the cement block and the crack was parallel to the surface of the implant (left of Figure 29). Again to offer a more complete inspection of the cracking in the cement mantel, the implant has been removed from the view, as has the mesh from the cement mantel.

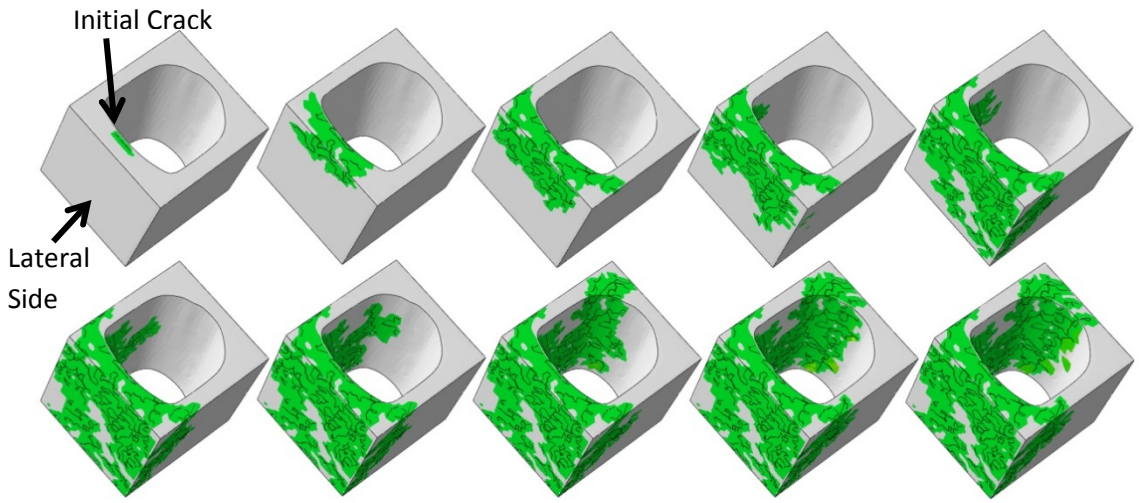

Figure 31: Crack Propagation.
Crack propagation for a parallel crack initiated on the lateral end of the cement mantel. Green represents elements that have experience cracking, and the major cracks have been visualized with a black line.

Evaluating crack propagation for other initial cracking conditions can be seen in Figure 32. In these two initial conditions the crack has been initialized perpendicular the surface of the implant; however one initial cracking location is on the anterior side, while the other is on the lateral side.

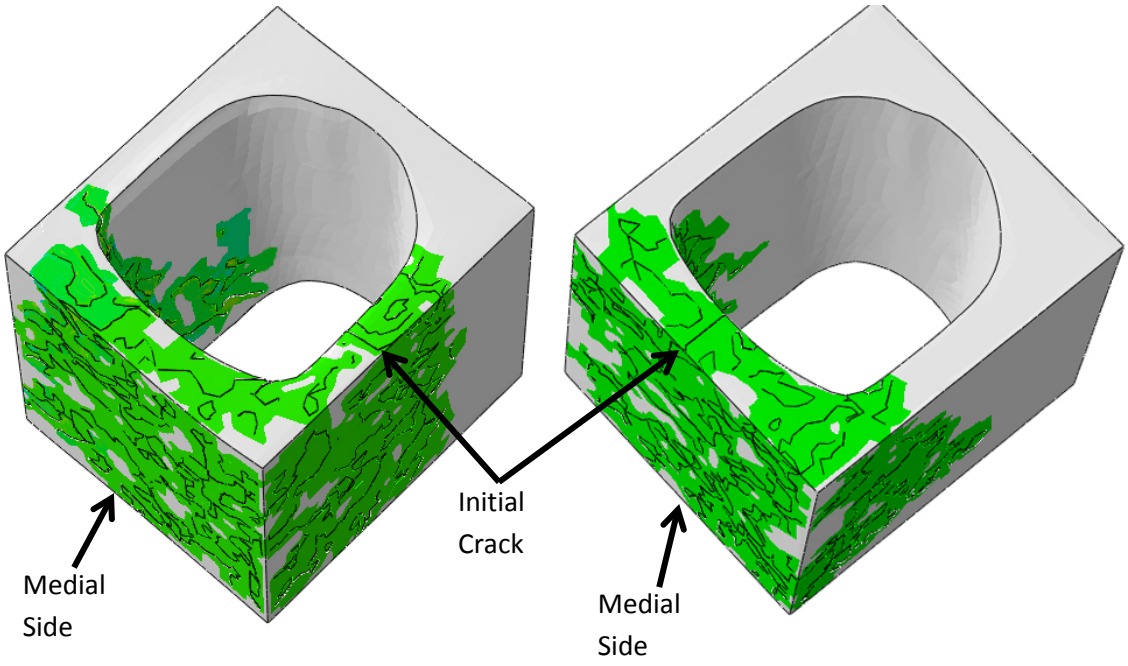

Figure 32: Final Crack Propagation.
Here are two final crack propagations for differing initial cracking location. On the left the crack was initialized perpendicular to the surface of the implant on the posterior side. Of the right the crack was initialized perpendicular to the implant on the posterior side.

In order to quantify the amount of cracking occurring in these different scenarios Figure 33Figure 33: is offered. In this graph a percent of nodes involved with cracking is offered. Since each model uses an identical mesh, this allows for a direct evaluation of each initial crack location.

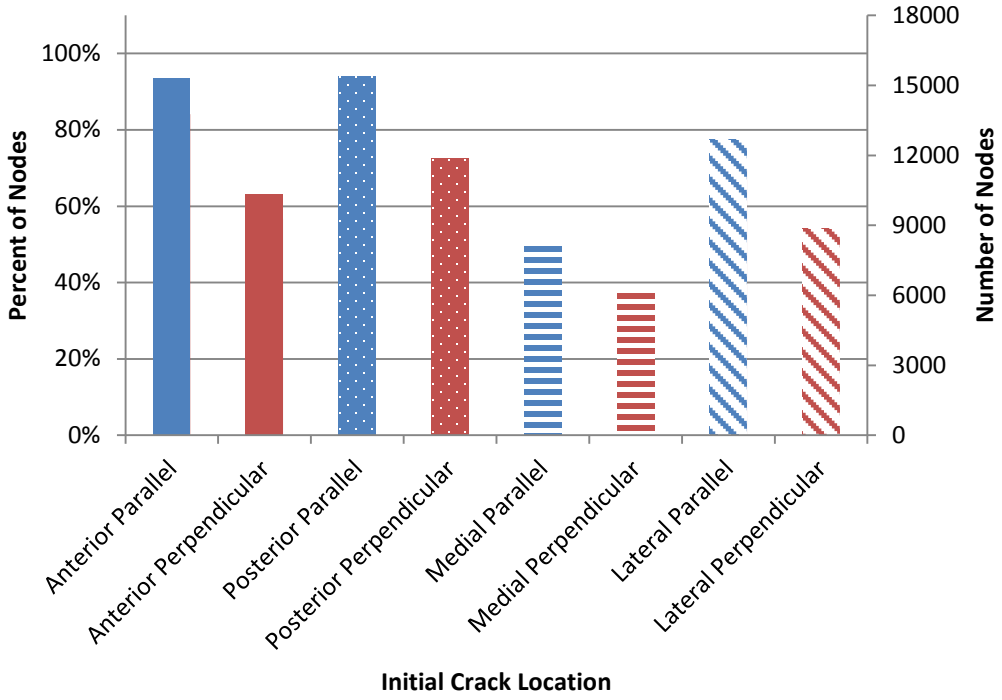

Figure 33: Nodes in Crack for Different Initial Crack Locations.
Shown in this figure is the percent of cracking seen in the cement mantel for different initial cracking locations and orientations. Blue represents parallel crack orientation while red represents perpendicular. Different fill patterns represent different crack locations. From this figure it can be seen that cracking propagates throughout the cement mantel regardless of orientation and location.

Lastly in an effort to quantify the effects of not hitting resonance and show how dampening can alter the effectiveness of this technique two additional models were run with half and quarter resonance vibrational frequencies (90*Hz* and 45*Hz*). These two models were evaluated for the optimal cracking configuration (initial crack located laterally and parallel to the implant). The cracking in these models has also been quantified by looking at the number of nodes involving crack and comparing them to the total number of nodes, blue bars in Figure 34. Additionally the set of nodes in each case is also compared to show how similar the crack propagation is between hitting the natural frequency and missing the natural frequency. For a comparison, the lateral perpendicular case has also been added to this graph.

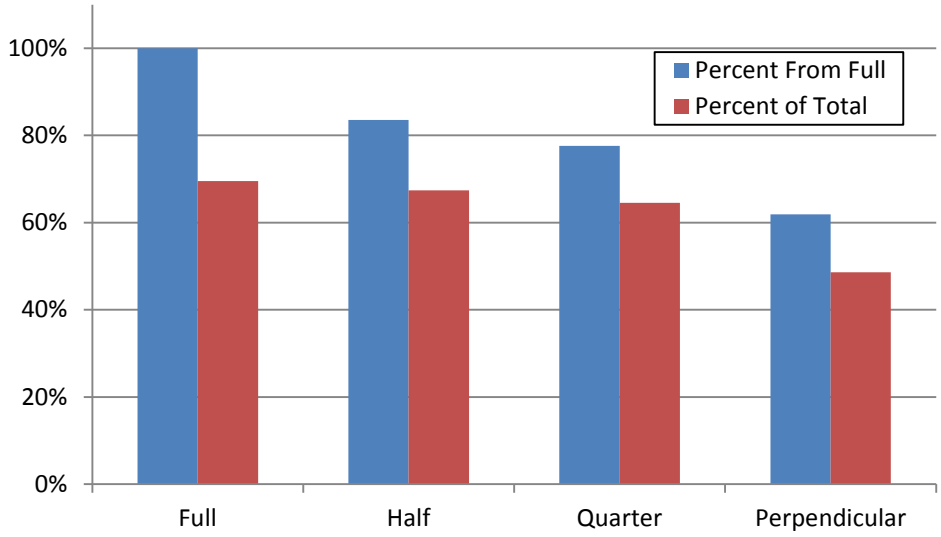

Figure 34: Nodes in Crack for Different Frequency Conditions.
Blue is the percent of nodes in crack also in the first mode cracking. Red is the percent of nodes in crack from the total number of nodes in the cement mantel.

4.3.4 Discussion

As can be seen in Figure 30 a crack will not nucleate and propagate on its own. When a crack is initiated crack will propagate throughout the cement mantel as shown in Figures 31 and 32. This study also shows crack initiation location has some bearing on crack propagation, where cracks initiated parallel to the surface of the implant propagate more easily. Additionally this model shows that hitting resonance will not prevent cracking from occurring, but rather limit the amount of cracking seen in the implant. It is hypotheses that this is due to resonance minimizing the dampening caused by the cement mantel; as the dampening falls the strains will increase leading to higher stresses and more cracking. Furthermore it is hypothesized that adding soft tissue, and bone to the system will cause more dampening making resonance a more important factor. As stands adding the cement mantel in this system has dampened the system by with a dampening ratio (ζ) of about 6.

Finally to show that crack propagation does not occur on the surface of the cement mantel alone, a cut view is offered in Figure 35. This figure shows the same scenario as Figure 31 (parallel crack initiated on the lateral end), however a cut view is offered to show that cracks propagate internally. In this figure green areas represent elements that have cracking, while white areas have no cracking. Since Abaqus does not allow for the crack path to be projected onto this view, the mesh is displayed.

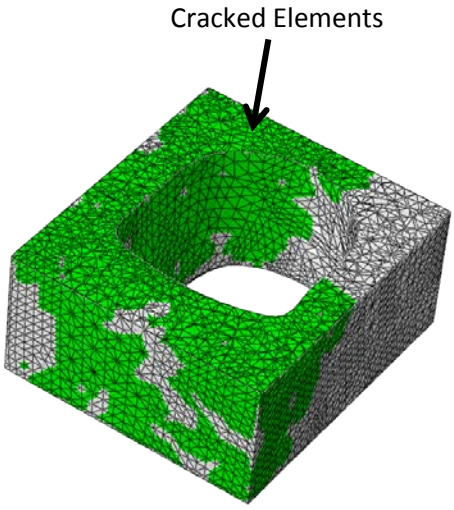

Figure 35: Cut View of Cement Mantel with Cracked Elements.
Cut view of the cement mantel where for a parallel crack initiated on the lateral end of the cement mantel. Green represents elements that have experience cracking. Black lines represent the elements and mesh on the cement.

4.3.5 Conclusions

The goal of the *in-silico* testing was to show that after determining an implant's natural frequency that vibrating that implant at its natural frequency will induce crack propagation. The proposed model successfully shows that if a crack is initiated in the cement mantel, regardless of location or orientation, using a low force mechanical vibration to put the implant into resonance results in crack propagation. The testing here also concludes that while putting the implant into resonance is not necessary to induce cracking, it increases the amount of cracking seen. The cracking demonstrated by this modeling is evenly distributed throughout the cement mantel, independent of crack location and a parallel orientation results in more cracking.

Because cracking needs to be initiated in the cement mantel it is hypothesized that the cracking will not propagate from the cement mantel into any surrounding bone stock in a clinical application.

CHAPTER 5 IN-VITRO TESTING

5.0 Introduction

The goals of this thesis are three fold: (i) characterization of natural frequencies for femoral implants, (ii) demonstrate that crack propagation can occur by putting an implant into vibrational resonance, and (iii) design a device that can apply controlled vibrational forces to an implant and easily integrate with current operating room equipment. Up to this point *in-silico* testing has been used to achieve the first two goals of this thesis. *In-vitro* testing will be discussed in this chapter and is aimed at designing a device that can put an implant into mechanical resonance, and easily assimilate with current rTHA equipment and techniques. The *in-vitro* testing consists of three parts (i) the conceptualization and building of the device (ii) a study to calibrate the speed of the device to speed input and load and (iii) testing of the device to confirm the hypothesis of that vibrations can be used to debond an implant from a cement mantel. In this section each of these topics is explored in detail. Section 5.1 will discuss the final design of the prototyped device and how each feature was picked. Section 5.2 explores the relationship between the device inputs, mass moment of inertia and speed settings, and the output vibrational frequency of the device. Lastly, Section 5.3 brings together all the information discussed in this thesis in an experimental validation of the *in-silico* testing as well as provides an initial testing ground for the prototyped device.

5.1 Device Design

The premise of this project is to vibrate an implant loose of its position in PMMA. To do this a device needs to be built to create controlled vibrations. Several design factors must be considered in designing an effective device: (i) generation of vibration, (ii) vibration frequency (iii) vibrational force and (iv) minimal vibrational energy loss. Several methods exist to create vibrations such as linear perturbation with an actuator, use of a function generator and off balance rotation [7]. The goal of the project, however, is to develop a tool that can easily interface with current surgical devices. During an rTHA a surgeon already has a vast array of power tools available, so this design was intended to be an attachment to a variable speed surgical drill. A surgical drill can provide the necessary range of speeds in terms of frequency as defined in Section 4.1, as well as provide an easy way to generate vibrations through off balance rotation. Since surgical drills are expensive, and any motor with the required speed output (over 150*Hz* or 56000*RPM*) can be used, this validation study uses a wood working router to mimic the intended surgical drill. The router used in this design is a 1.5*HP* Chicago Electric Power Tools variable speed router [57]. The motor in this router is reported by the manufacture to have speeds between 450*Hz* for no load and 180*Hz* for high loads.

In general the device is a custom router bit with an off balanced moment of inertia created by an attached counter weight. Here one vibrational cycle is created with each revolution of the bit. In order to transmit the vibrational energy to the implant a custom collar has been designed to fit to the implant and allow the router bit to be inserted. This design can be seen in Figure 36.

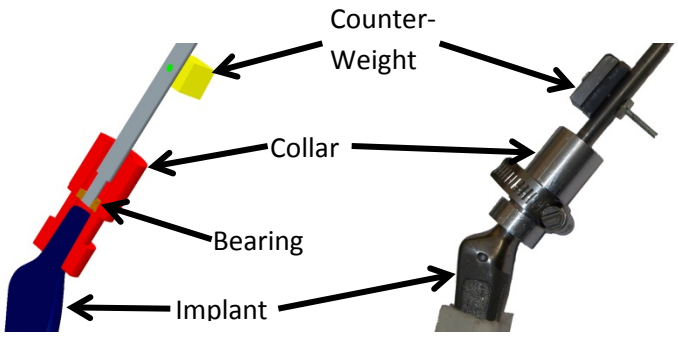

Figure 36: Prototype Design.
On the left, blue is the implant, red is the collar, gold is the bearing, grey is the router bit, yellow is the counterweight, green is the screw holding the counterweight. On the right is the actual device implementation.

Another significant design factor of consideration included magnitude of vibration control. To effectively control the magnitude of the generated vibrational force, the router bit is to be off balanced using interchangeable weights. In this way when if a known force is desired for a specific mode, then the required mass of the weight can be calculated with Equation (7).

$$m \cdot r = \frac{F}{4\pi^2 f^2} \qquad (7)$$

In this equation, F is the desired force, f is the natural frequency measured in Hertz, m is the mass of the counter weight and r is the distance from the center of the counter weight to the center of rotation. In order to accommodate the high speeds of over 200*Hz* or 12,000*RPM* a thrust ball bearing is used to interface the router bit with the implants collar. In this way the vibrational energy loss from friction is minimized, in addition it prevents energy loss from open mechanical connections. Due to the large torques and forces acting on the small router bit, this part was constructed out of steal. The bigger collar, would not feel the same stresses as the bit, so this part was constructed with aluminum. The distal end of the collar interfacing with the implant was designed to have the internal pitch as the implant. This matched pitch increase the surface area between the implant and collar and allows for hose clamps to be used to hold the collar to the implant. Finally the collar has been fitted with four relief cuts on the implant end,

this allows for collar to deform slightly to fit multiple implants rather than one collar per implant.

5.2 Device Calibration

5.2.1 Introduction

A vibrational force must be induced at the same frequency as one of the natural frequency modes of the implant in order for the device to use a natural frequency as a means of extraction. With the proposed device a router with an unbalanced bit is being used to generate the vibrational force. For this reason a calibration between the speed setting on the router and the actual speed of the bit, as well as the changing mass moment of inertia must be performed. In this section, the full details of this calibration are provided, it will start with a description of the devices used, next the methods and calibration protocol will be discussed, and finally the results will be presented and discussed.

5.2.2 Instrumentation

This section will describe the instrumentation needed to perform this calibration (Table 3), how the components of the device are attached and hardware and software used during device calibration.

Table 3: Required Parts for Device Speed Calibration.

Item	Number needed
1-1/2 HP Variable Speed Plunge Router (Chicago Electric)	1
Encoding Wheel	1
Router Bit	1
Weights	4
Arduino Uno	1
Photo Interrupter (GP1A51HRJ00F)	1

The router used in this study is a variable speed router [57], here speed control is offered via a dial that can be moved from zero to nine. This system has been altered with a more accurate measuring system in degrees. Every two degrees on the dial has been marked with a red line as shown in Figure 37.

Figure 37: Router Speed Control.
Shown here is the speed control knob on the router used in this experiment.

Attached to the router is the custom router bit, which allows for the attachment of both the counter weights and the encoding wheel. The router bit has been fitted with a threaded hole at A in Figure 38 so that the encoding wheel may be attached. Holes in the bit at B are used to attach counter weights allowing for the control of the mass moment of inertia.

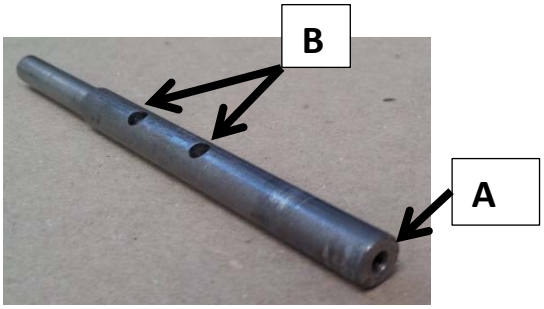

Figure 38: Custom Designed Router Bit.
Here is the custom designed router bit. The threaded hole at A is for the attachment of a encoding wheel. The holes at B are used to attach counterweights.

The encoding wheel (Figure 39) is made of an aluminum substrate with a diameter measuring approximately 2.5*in*, and $^{1}/_{16}$*in* thick. A radial notch was cut into the disk approximately one-eighth of an inch deep and extending 20 degrees. To reduce the chance of light scattering causing false readings, the encoding wheel was given a non-reflective veneer.

Figure 39: Encoding wheel.
Shown here is the encoding wheel used for calibration.

A photointerrupter [58] is a sensor consisting of an infrared (IR) emitter and detector. When an object is placed between the two, the IR source is unable to get to the detector and the detector sends an “OFF” signal. On the other hand when no object is placed between the emitter and detector, the detector will return an “ON” signal. The photointerrupter requires power for both the emitter and detector, which can conveniently be provided by a micro controller.

The Arduino Uno [59] is the microcontroller used for this calibration. It is used to provide the photointerrupter power, as well as record and interpret the signal. The Arduino is loaded with custom written C code, to read the signal from the photointerrupter and convert this signal timing into the speed of the router, which is provided in Appendix B. In order to connect the photo interrupter to the Arduino circuitry had to be designed and built, the wiring diagram used for this circuitry is supplied in Appendix C.

As a system, the router bit is connected to the router, and then encoding wheel is attached to the bit. The photointerrupter is then mounted onto the router so that as, the encoding wheel rotates, the timing between rotations can be measured with the photointerrupter and Arduino (Figure 40).

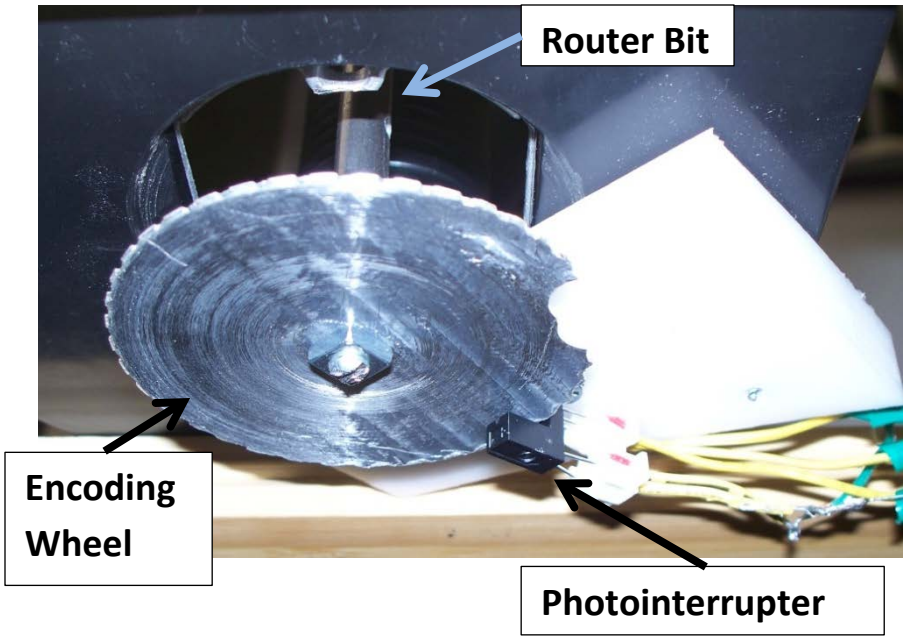

Figure 40: Calibration System. Here is the calibration setup.
The router bit is inserted into the router, and the encoding wheel attached to the bit. The photointerrupter is placed so that the notch in the encoding wheel will interrupt the IR signal when the notch is not in the photointerrupter.

5.2.3 Methods

To perform device calibration, the output variable, speed, is measured while incrementing the input variables, counter weights and speed control setting, separately. To carry out the calibration, the device was setup as previously described in Section 5.2.2. Initially no counter weights were applied and the computer was turned on to record data. Router settings began at an angle of 0° and were complete once 20° was achieved at a two degree resolution so that 10 calibration points could be obtained for each moment of inertia. Each calibration run consisted of turning the router on and recording the speed for a minimum of 30 seconds; later post processing would reveal the steady state speed of the router. Mass moment of inertia for the router bit was calculated with Equation (8). This equation assumes that the weights are perfectly square allowing for the basic calculation of mass moment of inertia. Since these weights are offset from the center of rotation, the parallel axis theorem is also used in Equation (8).

$$I = \sum_{i=1}^{n} \frac{1}{12} m_i \left(l_i^2 + w_i^2\right) + m_i r_i^2$$
$$where \quad (8)$$
$$r_i = \frac{d_i}{2} + \sum_{j=1}^{i-1} d_j$$

Here I is the mass moment of inertia, m is the mass of the weight, r is the moment arm, and w is the width of the weight, l is the length of the weight and d is the depth of the weight. To prevent the uncontrollable shaking of the device, counter weights were matched up based on mass moment of inertia and placed 180° out of phase. This balance considerably reduced the vibration of the machine during calibration. The calibration was performed at three torsional loads providing for 30 data points for this calibration.

5.2.4 Results

Data was collected in the form of a time domain step response (Figure 41), i.e. recording the speed as a function of time when the device is turned on. The results of these step responses are that steady state speed for all settings was reached. Steady state speeds were determined by using a maximum criterion. Since the data is smooth and very flat at steady state speeds the system is considered over damped (e.g. has no over shoot) [60]. Since this is an over damped system, a maximum criterion is an acceptable means of calculating the steady state value.

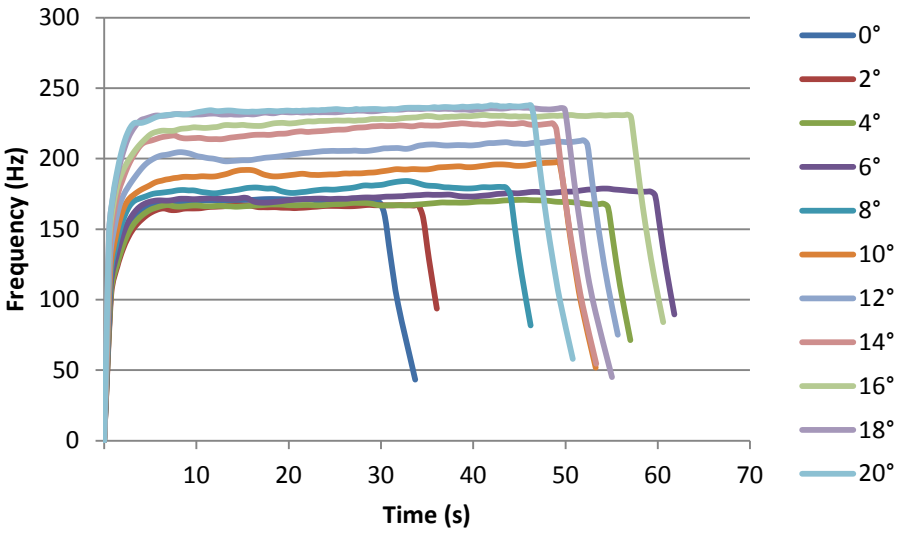

Figure 41: Calibration Raw Data.
Shown here is the raw calibration data for a torsional load of 0, here the x axis is time, the y-axis is the router speed measured in frequency, and each line represents a different router speed setting measured in degrees.

Evaluating steady state speeds as a function of router speed setting, a calibration curve can be obtained (Figure 42). Calibration curves can also be evaluated as a function of mass moment of inertia by plotting each mass moment of inertia curve on the same plot. This has also been performed in Figure 42. From the data it can be seen that the relationship between speed and input speed angle can be approximated as linear at a 2° resolution. At a higher resolution this same assumption is no longer valid.

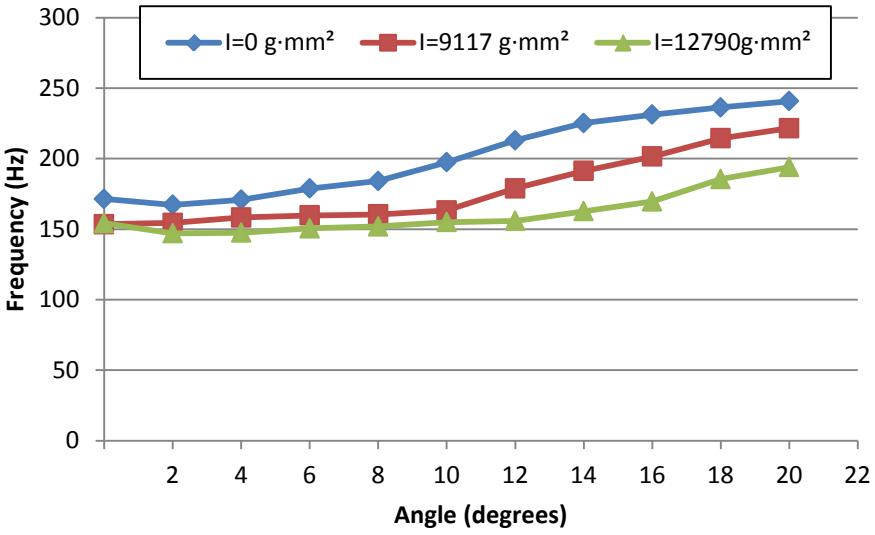

Figure 42: Calibration Results.
Shown here is the steady state speed recorded as frequency plotted against router input angle. Each colored line is for differing moment of inertias. As the input angle increases, so too does the steady state speed. When the moment of inertia is increased, then the output speed decreases from the router.

Another way to evaluate the time response of the device is to look at the rise time. The rise time is the time required for the speed to go from 10% to 90% of its steady state value [60]. The rise time was computed for the calibration data and is presented in Figure 43. Rise time for the device fell between 1 and 5.5*s (*Figure 43). This means that when the device is used, it must be on for a minimum of 5.5 seconds before a resonant frequency can be attained.

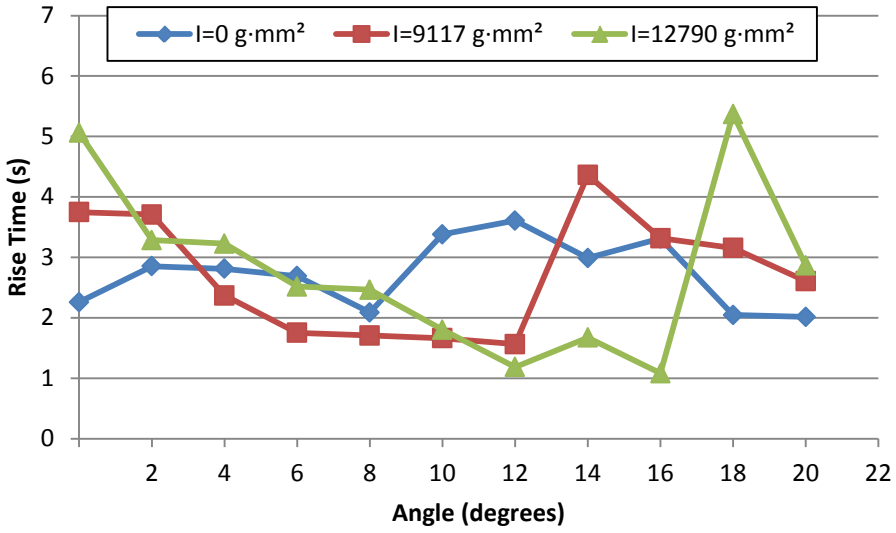

Figure 43: Calibration Rise Time.
Plotted here is the rise time, or time it takes to rise from 10% to 90% of the steady state peak. All times fall between 1 and 5.5 seconds. For this reason the device must be turned on for at least 5.5 seconds before a steady state speed is achieved.

5.2.5 Conclusion

This study has successfully calibrated the router input angle and applied torque to the output speed. It has been shown that rise time is at most 5.5*s*. Furthermore, the calibration data does not linearly relate output speed to input angle or mass moment of inertia. For a small scale, however, linear interpolation can be used to calculate the required input angle for a given inertial load and desired output speed.

5.3 In-vitro Testing

5.3.1 Introduction

After the device design and calibration, the next step is to validate the *in-silico* results with *in-vitro* testing. In this section an experiment is performed using the implant cement mantel setup used in the *in-silico* testing from Section 4.3. The implant is first surrounded by a cement mantel, and the prototyped device is then used to extract the implant. Since *in-silico* testing revealed that cracking would only propagate if first initiated, this is the expected result from the experimental testing. This section describes in detail experimental setup, including implant/cement preparation, natural frequency determination, and device setup. This section will then conclude with a characterization of the experimental results and device design.

5.3.2 Methods

For the experimental setup it was decided to surround the implant in bone cement in the middle region. This was because the middle region had a porous coating, which would allow for maximum fixation. Additionally, the height of the cement mantel was chosen to be 25*mm* as this would put the natural frequency (180*Hz*) within the operating range of the router. The natural frequency of the implant for this boundary condition was determined using the methods described in Section 4.1 and 4.2. Additionally, the smaller implant was chosen for this experiment as it was an easier implant to physically ground the anterior and posterior ends of the cement mantel, thus matching the *in-silico* conditions used in Section 4.3, Figure 24.

In order to encase the implant with this specific amount and location of PMMA, a custom built mold was used. After the PMMA was mixed it was poured into the mold and the implant was placed within mold and allowed to cure. In order to get the proper cement mantel thickness, the mold was built such that the inner dimensions measured 25x28x50*mm* and was made of a translucent polycarbonate. This allowed for the cement mantel to be viewed and altered before curing, enabling precise creation of the cement mantel.

The Zimmer Dough-Type PMMA bone cement used consisted of a bone cement powder [61] and a methyl methacrylate monomer [62]. To create the bone cement, 40*g* of the bone cement powder was poured into a bowl, next 20*cc* of methyl methacrylate monomer was added to the bowl. This mixture was slowly mixed for several minutes until an even consistency was obtained. After the bone cement and implant were added to the mold, the cement was allowed to cure for 24 hours before being extracted from the mold (Figure 44).

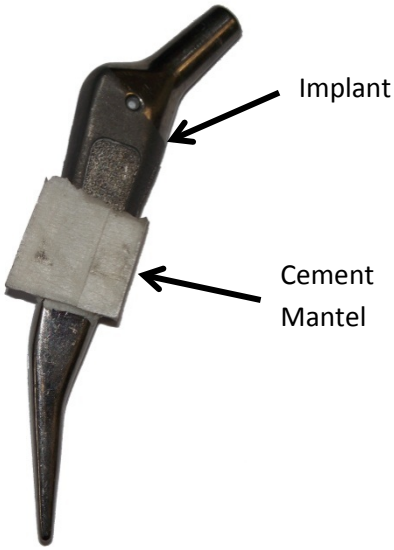

Figure 44: Implant Surrounded by Cement Mantel.
Here is the implant used in the experimental validation study. The implant has been surrounded by a small cement mantel located in the middle of the implant.

To verify the *in-silico* results, first the experimentation was performed without initiating a crack. Next, the implant was fitted with the collar and router bit, with a 60*g* mass counterweight. Since this is the same setup as is used in Section 4.2, the natural frequency for this boundary condition had already been calculated as 200*Hz*. The natural frequency was used in conjunction with the calibration data to determine that the required router speed setting was 12.5°. The router was set to this setting, and the router bit connected to the router. Finally, a vice was used to clamp the anterior and posterior sides of the cement mantel, giving the same boundary condition used in section 4.2 and shown in Figure 45. This experimental setup is also

similar to the calibration setup. In this case the counter weights are not placed out of phase, and the distal end of the router bit is connected with the collar as opposed to the encoding wheel.

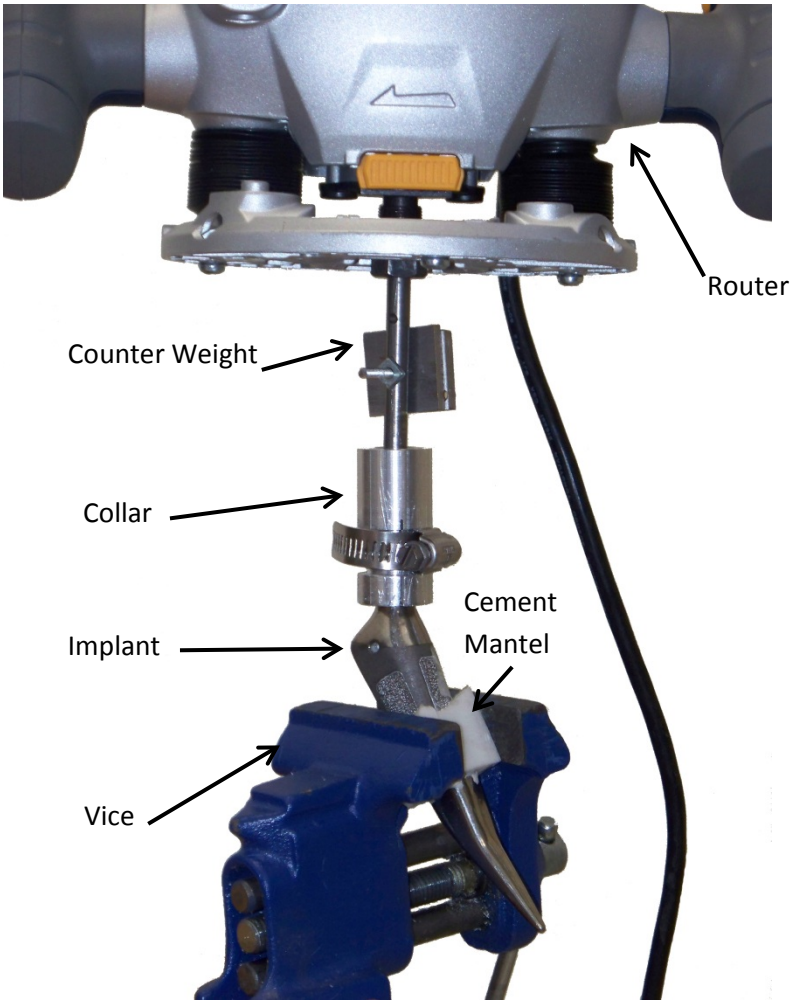

Figure 45: Experimental Setup.
Here is the experimental setup for the in-vitro testing. The implant was fitted with the collar and the counter weights attached to the router bit. The router was then attached to the router bit before the cement was clamped down with a vice.

Once the experimental preparation was complete, the router was turned on and held there for a full minute, to ensure the router setting was adequate. This process was repeated with higher and lower router settings (±1 degree or ±15*Hz*) for several minutes. After several minutes the router was turned off and the system disassembled so that the cement mantel could be evaluated.

As predicted by the *in-silico* testing, without first initialization of a crack, no cracking was observed in the cement mantel. In order to perform the experiments with an initialized crack, cracks were initiated in the cement mantel with a chisel. To initialize the crack the chisel was placed on the lateral end of cement mantel (most observed cracking from *in-silico* testing) and then struck with a hammer. When the hammer struck the chisel, cracks were both initiated and propagated at the same time. Rather than initiating a small crack in the cement mantel, large pieces of the cement broke off.

5.3.3 Results

During testing it was observed that the vibrational force steadily increased for several seconds before reaching a steady state condition as predicated by the calibration study. Additionally, by placing a hand on the implant it could be felt that a vibration was being induced on the implant. When the system was disassembled no cracking was seen when a crack was not first initialized. As stated in the methods section, a crack was then initialized with a chisel; however this was not successfully performed. When a hammer hit the chisel, large pieces of the cement mantel broke off, as opposed to initiating a crack.

5.3.4 Discussion

In-vitro testing successfully showed that the proposed device can converted rotational energy into a vibrational energy which was then transferred to the implant. However cracking as predicted in Section 4.3 was not seen. In Section 4.3 it was shown that if a crack is not first initiated into the cement mantel, then the forces generated by the vibration are not large enough to nucleate a crack in the cement mantel. If a crack is not first nucleated, *in-silico* testing showed that cracking would not be seen. As such no cracking was observed in the *in-vitro* testing, without initiating a crack. In order to initiate a crack in a manner that can be easily performed in a surgical setting, a chisel was used to initiate a crack. When the chisel was used, it

was able to both initiate and propagate a crack though the cement mantel such that large pieces of cement would break off. While easy propagation of a crack is an attractive quality for removing the cement mantel with a vibrational force, this leaves a problem of how to easily and effectively initiate a crack in a clinical setting. It is possible that a smaller chisel or even an osteotome may work better for the initiation of a crack; however none were available at the time of testing. Additionally, it may be possible that having a bonded interface on both sides of the cement mantel may help keep a chisel from splitting the cement mantel and simply initiate a crack.

Furthermore, in a vast majority of patients undergoing an rTHA the failure mode of the implant is loosening. This is typically caused by fatigue cracking within the cement mantel from day to day use. In this case the desired crack initiation for this device would already exist, thus no external method of initiating a crack would be necessary. Incorporating this means of initiating a crack is a difficult procedure that is outside the scope of this project.

5.3.5 Conclusions

As demonstrated in *in-silico* testing initiating a crack in the cement mantel is critical to the propagation of the crack in the cement mantel. Current implementations of *in-vitro* testing do not adequately initiate a crack for the proposed device to propagate a crack through the cement mantel. Future work needs to be heavily focused on the initiation of a crack in the cement mantel in a clinically relevant manner. The current design of the device, however is easily implementable in a surgical setting, and has successfully transferred vibrational energy into the implant.

CHAPTER 6 SUMMARY, CONCLUSIONS, LIMITATIONS & FUTURE WORK

6.1 Summary

Each year an estimated 50,000 rTHAs are performed, and this number is estimated to more than double in the next 17 years [2]. Revision surgeries become necessary for a variety of reasons, the most common of which are implant loosening and infection. Current medical techniques for removing femoral implants require invasive operations and are time consuming, costly and require expert surgical skill under the best of scenarios. As a result the medical community is constantly looking for and evaluating new techniques to perform rTHAs. The long term goal of this project is to provide significant advantages over current surgical procedures, by utilizing an implant's natural frequency to debond the implant from its surrounding bone cement mantel. Allowing an implant to be removed in an easier, less skilled manner, it is proposed to put the implant into its mechanical resonance, to debond the implant from the surrounding PMMA cement mantel.

This long term goal has paved the way for three short term goals this thesis aimed to achieve. The first goal was to characterize the design parameters which affect the natural frequency of an implant. The second was to demonstrate that crack propagation is achievable using low amplitude mechanical vibrations acting on an implant at its natural frequency. The third and, final goal was to develop a device which is able to (i) easily integrate with current operating room devices, and (ii) transfer a wide variety of commercially available implants.

In order to determine the factors affecting an implant's natural frequencies *in-silico* testing was used. Through *in-silico* modeling it was determined that the natural frequency of an implant is strongly dependent on its geometry, boundary conditions and material properties. If the geometry and boundary conditions are held constant, then the effects of the material properties can be described. Furthermore, effects attributed to geometry can mainly be accredited to the size of the implant, since implants generally have a similar form. Due to the

similarities in shapes the first three natural frequency modes correlate to anatomical position. The modes correlation is as follows: mode one represents anterior posterior motion, mode two corresponds to medial later motions and mode three equates to a torsional rotation on the transverse plane.

In order to show that crack propagation is possible with low amplitude vibrations (goal two), first simulating an implants response to its natural frequency is required. It has also been shown that an implant perfectly bonded to a cement mantel can be modeled with tie constraint. Additionally the simulation of a vibrational perturbation can be obtained with a cyclic dynamic load rotating at the natural frequency. When the embedded implant is operated at its natural frequency a positive feedback like system is not obtained; this is attributed to the cement block acting as a dampener ($\zeta \approx 6$). The resulting deformation on the femoral neck initially has a large amount of overshoot in the direction of the initial loading. After several vibrational cycles, however, the overshoot dampens out resulting in a near perfect circular deformation path as would be expected. Peak stress values in the cement mantel occur at the sides with which boundary conditions have been placed, and these values are smaller than required to initiate a crack in PMMA. For this reason it has been hypothesized that a crack will have to be externally nucleated to see crack propagation.

Finally, on the computational side, it has been shown that crack propagation will not occur unless the crack is first nucleated. Once a crack has been initialized regardless of its location it will propagate throughout the cement mantel, both internally and on the surface, when the implant is vibrated at its natural frequency. Additionally, it has also been shown that not putting the implant into resonance does not prevent cracking, but rather resonance increases the level of cracking. It is speculated that this increased cracking at resonance is due to resonance decreasing the dampening effects in the system; as more dampening is added to the

model in the form of bone and soft tissue this will become a more critical factor. This marks the achievement of the second goal, in-*silico* testing has dominated that crack propagation is achievable by placing an implant into resonance. Additionally, since the cracking requires an externally nucleated crack, it is hypothesized that the surrounding host bone would be unaffected by the cracking in the cement mantel. Since stress levels in the cement mantel do not exceed 15*MPa*, crack nucleation and propagation will not occur in the host bone. This would make the proposed operating technique both safe and require little technical surgical skill to perform.

The third and final goal, is to develop a device which can (i) easily integrate with current operating room device and (ii) transfer vibrational energy into an implant. To create the device that can generate the required controlled vibrations an interchangeable device has been designed. This device operates on the principle that spinning on object though an axis other than one that goes through its center of mass causes a vibration. The device has been designed to operate with any motor that can provide a rotational speed output of over 180*Hz* (6500*RPM*). This system has also been designed with a collar which can fit a variety of implants and sizes.

The device design is intended to be used with a variable speed surgical drill; however for the purposes of testing a variable speed router has been used. Speed calibration has been performed using an Arduino Uno, a photointerrupter and an encoding wheel to time the frequency with which the router can revolve under varying loading conditions. The calibration shows regardless of the desired speed, a steady state speed is reached within 5.5 seconds. The calibration also showed that a two degree resolution of the router speed setting provides adequate data so that linear interpolation can be used to estimate the operating speed of the motor. Additionally the calibration showed that the operating speed has a large dependency on

the mass moment of inertia, however linear interpolation can be used to predict the effects of differing loads.

Lastly *in-vitro* experimentation was performed; this interchangeable device successfully transferred the generated vibrational energy to the implant. *In-vitro* testing, however, was unable to validate the predicted *in-silico* cracking. This is hypothesized to be the result of inadequate crack initiation. Current methods for initiating a crack involve using a carpenter's chisel and a hammer. This method was successful in initiating a crack; however it also propagated the crack so that pieces of the cement would break off. It has been proposed that a better mechanism for initiating a crack would be beneficial, as could the use of larger weights on the router bit.

6.2 Limitations & Future Work

The current implementation of the FE models accounts for crack propagation only though a maximum critical stress criterion. Future models should incorporate crack growth through other factors: first and foremost though fatigue, and lastly through time dependent factors such as creep. Furthermore, modeling was only performed for a system consisting of an implant and a cement mantel. Future models should also incorporate bones, and surrounding soft tissues.

The *in-silico* modeling was definitive; once a crack was initiated the crack thoroughly propagated through the cement mantel. For this reason it is hypothesized that a more effective crack initiation technique would result in similar *in-vitro* cracking. A crack initiation tool should be designed and utilized in future testing. Additionally, calibration utilizing heavier weights should be performed as a higher load may be better able to propagate cracks.

6.3 Conclusions

As explained in the motivation, three main goals exist for this project. First is to characterize significant implant design parameters which affect the natural frequency of an implant using computation modeling. This has been performed and is discussed in section 4.1. Results show that affects attributed to the material properties can be calculated, while the fixation level or boundary conditions are the major contributors of changing natural frequency modes. Since most implants are of the same shape, the size of the implant is also a factor in determining the natural frequency modes, where a smaller more affixed implant results in higher natural frequency modes.

The second goal of the project is to demonstrate cement crack propagation utilizing a low amplitude mechanical vibration. *In-silico* modeling has successfully shown crack propagation in the cement mantel using XFEM. The computational modeling shows that without first initiating a crack, no crack nucleation occurs. Once a crack is initialized, however, the crack will easily propagate though nearly the entire cement mantel. Furthermore *in-silico* testing also showed that cracks will also propagate if the implant is not in resonance, but that hitting resonance increases the amount of cracking. It is hypothesized that this can be attributed to the reduced dampening observed at resonance. As the assumptions in the model decrease, by adding the bone and soft tissue, the dampening affects will become larger making resonance more important. While *In-vitro* testing did not verify the *in-silico* results, this is attributed to inadequate crack initiation.

The third goal was to design a prototype device that can (i) integrate easily with current operating room devices, and (ii) transfer vibrational energy to a wide variety of commercially available implants. The designed device has been devised to operate with any motor that can provide the necessary output speed. In this way the device can be easily transferred from a

router (as used in this thesis) to any surgical drill. Additionally the device has been successfully tested such that the kinetic energy of the motor is converted to a vibrational energy with the device and is then transferred to the implant though the use of a collar. The designed collar may need to come in several sizes in order to interface with any implant; however the collar is a simple design that can be easily manufactured.

Works Cited

[1] Hall, S. J., 2012, *Basic Biomechanics*, McGraw-Hill, New York, NY.

[2] Kurtz, S., Ong, K., Lau, E., Mowat, F., and Halpern, M., 2007, "Projections of Primary and Revision Hip and Knee Arthroplasty in the United States from 2005 to 2030," J Bone Joint Surg Am, 89(4), pp. 780-5.

[3] Berger, R. A., Jacobs, J. J., Meneghini, R. M., Della Valle, C., Paprosky, W., and Rosenberg, A. G., 2004, "Rapid Rehabilitation and Recovery with Minimally Invasive Total Hip Arthroplasty," Clinical Orthopaedics and Related Research, 429(pp. 239-247 10.1097/01.blo.0000150127.80647.80.

[4] Wang, A., Ackland, T., Hall, S., Gilbey, H., and Parsons, R., 1998, "Functional Recovery and Timing of Hospital Discharge after Primary Total Hip Arthroplasty," Australian and New Zealand Journal of Surgery, 68(8), pp. 580-583.

[5] Philpot, T. A., 2013, *Mechanics of Materials : An Integrated Learning System*, Wiley, Hoboken, N.J.

[6] Ugural, A. C., and Fenster, S. K., 1995, *Advanced Strength and Applied Elasticity*, Prentice Hall, Upper Saddle River, N.J.

[7] Rao, S. S., 1990, *Mechanical Vibrations*, *Addison-Wesley Series in Mechanical Engineering*, Addison-Wesley, Reading, Mass.

[8] Timoshenko, S., 1983, *History of Strength of Materials : With a Brief Account of the History of Theory of Elasticity and Theory of Structures*, Dover Publications, New York.

[9] Cannon, J. T., and Dostrovsky, S., 1981, *The Evolution of Dynamics : Vibration Theory from 1687 to 1742 : With 10 Illustrations*, *Studies in the History of Mathematics and Physical Sciences*, Springer-Verlag, New York.

[10] Glassman, A. H., and Engh, C. A., 1992, "The Removal of Porous-Coated Femoral Hip Stems," Clin Orthop Relat Res, 285), pp. 164-80.

[11] Dobzyniak, M., Fehring, T. K., and Odum, S., 2006, "Early Failure in Total Hip Arthroplasty," Clin Orthop Relat Res, 447(pp. 76-8.

[12] Springer, B. D., Fehring, T. K., Griffin, W. L., Odum, S. M., and Masonis, J. L., 2009, "Why Revision Total Hip Arthroplasty Fails," Clin Orthop Relat Res, 467(1), pp. 166-73.

[13] Taylor, J. W., and Rorabeck, C. H., 1999, "Hip Revision Arthroplasty. Approach to the Femoral Side," Clin Orthop Relat Res, 369), pp. 208-22.

[14] Masri, B. A., Mitchell, P. A., and Duncan, C. P., 2005, "Removal of Solidly Fixed Implants During Revision Hip and Knee Arthroplasty," J Am Acad Orthop Surg, 13(1), pp. 18-27.

[15] Ratner, B. D., 2004, *Biomaterials Science : An Introduction to Materials in Medicine*, Elsevier Academic Press, Amsterdam ; Boston.

[16] Zimmer, 2013, Versys Hip System April 3, 2013, http://www.zimmer.com/z/ctl/op/global/action/1/id/362/template/PC/prcat/P2/prod/y

[17] Taylor, R. H., Joskowicz, L., Williamson, B., Gueziec, A., Kalvin, A., Kazanzides, P., Van Vorhis, R., Yao, J., Kumar, R., Bzostek, A., Sahay, A., Borner, M., and Lahmer, A., 1999, "Computer-Integrated Revision Total Hip Replacement Surgery: Concept and Preliminary Results," Med Image Anal, 3(3), pp. 301-19.

[18] Paprosky, W. G., Weeden, S. H., and Bowling, J. W., Jr., 2001, "Component Removal in Revision Total Hip Arthroplasty," Clin Orthop Relat Res, 393), pp. 181-93.

[19] Sporer, S. M., and Paprosky, W. G., 2004, "Extended Trochanteric Osteotomy," Seminars in Arthroplasty, 15(2), pp. 113-118.

[20] Instruments, I. O., 2012, Revision Instruments, http://www.innomed.net/revision_curetteosteo.htm

[21] Lewis, G., 1992, "Effect of Lithotriptor Treatment on the Fracture Toughness of Acrylic Bone Cement," Biomaterials, 13(4), pp. 225-9.

[22] May, T. C., Krause, W. R., Preslar, A. J., Smith, M. J., Beaudoin, A. J., and Cardea, J. A., 1990, "Use of High-Energy Shock Waves for Bone Cement Removal," J Arthroplasty, 5(1), pp. 19-27.

[23] Plaut, R. H., 2008, "Snap Loads and Torsional Oscillations of the Original Tacoma Narrows Bridge," Journal of Sound and Vibration, 309(3-5), pp. 613-636.

[24] Varini, E., Bialoblocka-Juszczyk, E., Lannocca, M., Cappello, A., and Cristofolini, L., 2010, "Assessment of Implant Stability of Cementless Hip Prostheses through the Frequency Response Function of the Stem-Bone System," Sensors and Actuators a-Physical, 163(2), pp. 526-532.

[25] Taylor, W. R., Roland, E., Ploeg, H., Hertig, D., Klabunde, R., Warner, M. D., Hobatho, M. C., Rakotomanana, L., and Clift, S. E., 2002, "Determination of Orthotropic Bone Elastic Constants Using Fea and Modal Analysis," J Biomech, 35(6), pp. 767-73.

[26] Wahab, N., Soudki, K. A., and Topper, T., 2011, "Mechanics of Bond Fatigue Behavior of Concrete Beams Strengthened with Nsm Cfrp Rods," Journal of Composites for Construction, 15(6), pp. 934-942.

[27] Zhang, R., and Shi, Z. F., 2008, "Numerical Simulation of Rebar/Concrete Interface Debonding of Frp Strengthened Rc Beams under Fatigue Load," Materials and Structures, 41(10), pp. 1613-1621.

[28] Jeffers, J. R., Browne, M., Lennon, A. B., Prendergast, P. J., and Taylor, M., 2007, "Cement Mantle Fatigue Failure in Total Hip Replacement: Experimental and Computational Testing," J Biomech, 40(7), pp. 1525-33.

[29] Ramos, A., and Simoes, J. A., 2009, "In Vitro Fatigue Crack Analysis of the Lubinus Spii Cemented Hip Stem," Engineering Failure Analysis, 16(4), pp. 1294-1302.

[30] Ramos, A., and Simoes, J. A., 2009, "The Influence of Cement Mantle Thickness and Stem Geometry on Fatigue Damage in Two Different Cemented Hip Femoral Prostheses," Journal of Biomechanics, 42(15), pp. 2602-2610.

[31] Moaveni, S., 2008, *Finite Element Analysis : Theory and Application with Ansys*, Pearson Prentice Hall, Upper Saddle River, N.J.

[32] Logan, D. L., 2007, *A First Course in the Finite Element Method*, Thomson, United States.

[33] Hrennikoff, A., 1941, "Solution of Problems in Elasticity by the Frame Work Method," Journal of Applied Mechanics, 8(4), pp. 169-175.

[34] Huiskes, R., and Chao, E. Y., 1983, "A Survey of Finite Element Analysis in Orthopedic Biomechanics: The First Decade," Journal of biomechanics, 16(6), pp. 385-409.

[35] Wheeler, J. P., Miles, A. W., and Clift, S. E., 1997, "The Influence of the Stem-Cement Interface in Total Hip Replacement--a Comparison of Experimental and Finite Element Approaches," Proceedings of the Institution of Mechanical Engineers. Part H, Journal of engineering in medicine, 211(2), pp. 181-6.

[36] Stolk, J., Maher, S. A., Verdonschot, N., Prendergast, P. J., and Huiskes, R., 2003, "Can Finite Element Models Detect Clinically Inferior Cemented Hip Implants?," Clinical Orthopaedics and Related Research, 409), pp. 138-150.

[37] Stolk, J., Verdonschot, N., Cristofolini, L., Toni, A., and Huiskes, R., 2002, "Finite Element and Experimental Models of Cemented Hip Joint Reconstructions Can Produce Similar Bone and Cement Strains in Pre-Clinical Tests," Journal of Biomechanics, 35(4), pp. 499-510.

[38] Watanabe, Y., Shiba, N., Matsuo, S., Higuchi, F., Tagawa, Y., and Inoue, A., 2000, "Biomechanical Study of the Resurfacing Hip Arthroplasty: Finite Element Analysis of the Femoral Component," The Journal of arthroplasty, 15(4), pp. 505-11.

[39] Pastrav, L. C., Devos, J., Van Der Perre, G., and Jaecques, S. V., 2009, "A Finite Element Analysis of the Vibrational Behaviour of the Intra-Operatively Manufactured Prosthesis-Femur System," Medical engineering & physics, 31(4), pp. 489-94.

[40] 2012, *Abaqus/Cae User's Manual : Version 6.12*, Pawtucket, RI : ABAQUS,

[41] Achour, T., Tabeti, M. S. H., Bouziane, M. M., Benbarek, S., Bachir Bouiadjra, B., and Mankour, A., 2010, "Finite Element Analysis of Interfacial Crack Behaviour in Cemented Total Hip Arthroplasty," Computational Materials Science, 47(3), pp. 672-677.

[42] Perez, M. A., and Seral-Garcia, B., 2012, "A Finite Element Analysis of the Vibration Behaviour of a Cementless Hip System," Computer methods in biomechanics and biomedical engineering, pp.

[43] Agwai, A., Guven, I., and Madenci, E., 2010, "Predicting Crack Initiation and Propagation Using Xfem, Czm and Peridynamics: A Comparative Study," eds., pp. 1178-1185.

[44] Benvenuti, E., Tovo, R., Livieri, P., 2011, "A Brittle Fracture Criterion for Pmma V-Notches Tensile Specimens Based on a Length-Enriched Extended Finite Element Approach," Frattura e Integrita Strutturale, 17), pp. 23-31.

[45] Abaqus, 6.9, Dassault Systémes, Vélizy-Villacoublay, France, 2009.

[46] Rabczuk, T., Song, J. H., and Belytschko, T., 2009, "Simulations of Instability in Dynamic Fracture by the Cracking Particles Method," Engineering Fracture Mechanics, 76(6), pp. 730-741.

[47] Couteau, B., Hobatho, M. C., Darmana, R., Brignola, J. C., and Arlaud, J. Y., 1998, "Finite Element Modelling of the Vibrational Behaviour of the Human Femur Using Ct-Based Individualized Geometrical and Material Properties," Journal of biomechanics, 31(4), pp. 383-6.

[48] Winter, W., Mohrle, S., Holst, S., and Karl, M., 2010, "Parameters of Implant Stability Measurements Based on Resonance Frequency and Damping Capacity: A Comparative Finite Element Analysis," The International journal of oral & maxillofacial implants, 25(3), pp. 532-9.

[49] Non-Contact 3d Digitizer, vivid 910 Konica Minolta, Marunouchi, Chiyoda, Tokyo, Japan,

[50] Gemoagic Studio, 12.0, Geomagic Inc., Morrisville, North Carolina, 2010.

[51] Abaqus, 6.10-EF, Dassault Systémes, Vélizy-Villacoublay, France, 2010.

[52] Meyers, M. A., and Chawla, K. K., 2009, *Mechanical Behavior of Materials*, Cambridge University Press, Cambridge ; New York.

[53] Solidworks, 2010, Dassault Systemés, Vélizy-Villacoublay, France, 2010.

[54] Abaqus, 6.12.1, Dassault Systémes, Vélizy-Villacoublay, France 2012.

[55] Boger, A., Bohner, M., Heini, P., Verrier, S., and Schneider, E., 2008, "Properties of an Injectable Low Modulus Pmma Bone Cement for Osteoporotic Bone," Journal of Biomedical Materials Research Part B-Applied Biomaterials, 86B(2), pp. 474-482.

[56] Bayraktar, H. H., Morgan, E. F., Niebur, G. L., Morris, G. E., Wong, E. K., and Keaveny, T. M., 2004, "Comparison of the Elastic and Yield Properties of Human Femoral Trabecular and Cortical Bone Tissue," J Biomech, 37(1), pp. 27-35.

[57] 1.5 Hp Variable Speed Router, 67119, Chicago Electric Power Tools, Chicago, Illinois

[58] Photointerrupter, GP1A51HRJ00F, Sharp Microelectronics, Camas, Washington,

[59] Arduino Uno, Mouser Electronics, Mansfield, Texas

[60] Franklin, G. F., Powell, J. D., and Emami-Naeini, A., 2006, *Feedback Control of Dynamic Systems*, Pearson Prentice Hall, Upper Saddle River, N.J.

[61] Bone Cement Powder, Dough Type-Radiopaque, Zimmer, Warsaw, Indiana

[62] Copolymer Bonce Cement Liquid, Osteobond, Zimmer, Warsaw, Indiana

APPENDICES

Appendix A: Natural Frequency Calculation Tables

Table 4: Mesh Independence Study for Implant A.

Seed Size (mm)	Elements	Mode 1 (Hz)	Mode 2 (Hz)	Mode 3 (Hz)	BC
1	192638	3.3013	3.9772	21.497	1/3
2	41115	3.3057	3.9821	21.515	1/3
5	7927	3.3147	3.9933	21.58	1/3
10	5208	3.3194	3.9966	21.616	1/3
1	192638	29.937	49.234	126.51	2/3
2	41115	30.036	49.354	126.67	2/3
5	7927	30.276	49.364	127.28	2/3
10	5208	30.452	49.599	127.73	2/3
1	192638	46.374	70.856	142.7	Full
2	41115	46.446	70.904	142.78	Full
5	7927	46.908	70.383	143.27	Full
10	5208	47.158	70.443	143.67	Full

Table 5: Mesh Independence Study for Implant B.

Seed Size (mm)	Elements	Mode 1 (Hz)	Mode 2 (Hz)	Mode 3 (Hz)	BC
1	129076	13.311	15.682	86.543	1/3
2	25023	13.394	15.745	86.813	1/3
5	4228	13.614	15.951	87.763	1/3
10	1756	13.886	16.097	88.696	1/3
1	129076	181.85	193.5	423.47	2/3
2	25023	182.71	194.42	424.76	2/3
5	4228	185.43	197.42	429.9	2/3
10	1756	186.54	198.52	433.03	2/3
1	129076	361.19	363.76	1066.1	Full
2	25023	361.77	364.35	1066.7	Full
5	4228	363.84	366.43	1071.3	Full
10	1756	366.44	369.15	1078.4	Full

Table 6: Effects of Density on Implant A's Natural Frequencies.

Density (kg/m^3)	Modulus of Elasticity (GPa)	Poisson's Ratio	Mode 1 (Hz)	Mode 2 (Hz)	Mode 3 (Hz)	BC
2000	116	0.34	4.9585	5.9731	32.277	1/3
4500	116	0.34	3.3057	3.9812	21.518	1/3
6900	116	0.34	2.6696	3.2158	17.378	1/3
8000	116	0.34	2.4792	2.9866	16.139	1/3
2000	116	0.34	45.053	74.031	190.01	2/3
4500	116	0.34	30.036	49.354	126.67	2/3
6900	116	0.34	24.256	39.857	102.3	2/3
8000	116	0.34	22.527	37.016	95.006	2/3
2000	116	0.34	69.669	106.36	214.17	Full
4500	116	0.34	46.446	70.904	142.78	Full
6900	116	0.34	37.508	57.26	115.31	Full
8000	116	0.34	34.834	53.178	107.09	Full

Table 7: Effects of Density on Implant B's Natural Frequencies.

Density (kg/m^3)	Modulus of Elasticity (GPa)	Poisson's Ratio	Mode 1 (Hz)	Mode 2 (Hz)	Mode 3 (Hz)	BC
2000	116	0.34	20.093	23.617	130.22	1/3
4500	116	0.34	13.395	15.745	86.813	1/3
6900	116	0.34	10.818	12.715	70.108	1/3
8000	116	0.34	10.047	11.809	65.11	1/3
2000	116	0.34	274.07	291.64	637.13	2/3
4500	116	0.34	182.71	194.42	424.76	2/3
6900	116	0.34	147.56	157.01	343.02	2/3
8000	116	0.34	137.04	145.82	318.57	2/3
2000	116	0.34	542.66	546.53	1600.1	Full
4500	116	0.34	361.77	364.35	1066.7	Full
6900	116	0.34	292.16	294.24	861.45	Full
8000	116	0.34	271.33	273.27	800.03	Full

Table 8: Effects of the Modulus of Elasticity on Implant A's Natural Frequencies.

Density (kg/m^3)	Modulus of Elasticity (GPa)	Poisson's Ratio	Mode 1 (Hz)	Mode 2 (Hz)	Mode 3 (Hz)	BC
4500	116	0.34	3.3057	3.9821	21.518	1/3
4500	160	0.34	3.8823	4.6767	25.272	1/3
4500	225	0.34	4.6038	5.5459	29.969	1/3
4500	300	0.34	5.3161	6.438	34.605	1/3
4500	116	0.34	30.036	49.354	126.67	2/3
4500	160	0.34	35.275	57.964	148.77	2/3
4500	225	0.34	41.831	68.736	176.42	2/3
4500	300	0.34	48.302	79.37	203.71	2/3
4500	116	0.34	46.446	70.904	142.78	Full
4500	160	0.34	54.548	83.273	167.69	Full
4500	225	0.34	64.686	98.749	198.85	Full
4500	300	0.34	74.693	114.03	229.62	Full

Table 9: Effects of the Modulus of Elasticity on Implant B's Natural Frequencies.

Density (kg/m^3)	Modulus of Elasticity (GPa)	Poisson's Ratio	Mode 1 (Hz)	Mode 2 (Hz)	Mode 3 (Hz)	BC
4500	116	0.34	13.395	15.745	86.813	1/3
4500	160	0.34	15.732	18.491	101.96	1/3
4500	225	0.34	18.656	21.928	120.91	1/3
4500	300	0.34	21.542	25.32	139.61	1/3
4500	116	0.34	182.71	194.42	424.76	2/3
4500	160	0.34	214.59	228.34	498.85	2/3
4500	225	0.34	254.47	270.78	591.56	2/3
4500	300	0.34	293.84	312.67	683.08	2/3
4500	116	0.34	361.77	364.35	1066.7	Full
4500	160	0.34	424.88	427.91	1252.8	Full
4500	225	0.34	503.85	507.44	1485.6	Full
4500	300	0.34	581.79	585.94	1715.4	Full

Appendix B: Code used on the Arduino for Calibration

```
volatile int state = LOW;            // Boolean variable for sensor
unsigned long pulseTime,lastTime;    // variables to store time
int inputPin = 3;                    // input pin on the Arduino
int count=0;                         // count of how many switches have been made
int cmax = 80;                       // number of counts before displaying speed

void setup()                         // setting up the program
{
 Serial.begin(9600);                 // required for running
 Serial.println("starting");         // display to let user know program has started
}

void loop()                          // loop that program will run
{
        if(state != digitalRead(inputPin))// if the sensor has switch cases
        {
                count++;                        // increase count
                state = !state;                 // switch previous state of sensor
                if(cmax == count)               // if max number of counts before display
                {
                        count = 0;              // reset count
                        lastTime = pulseTime;   // set the previous time (microseconds)
                        pulseTime = micros();   // get the current time  (microseconds)
                                                // display speed in Hz or RPS
                        Serial.println(1000000.0*cmax/((pulseTime-lastTime)*2.0));
                }
}
```

Appendix C: Wiring Diagram

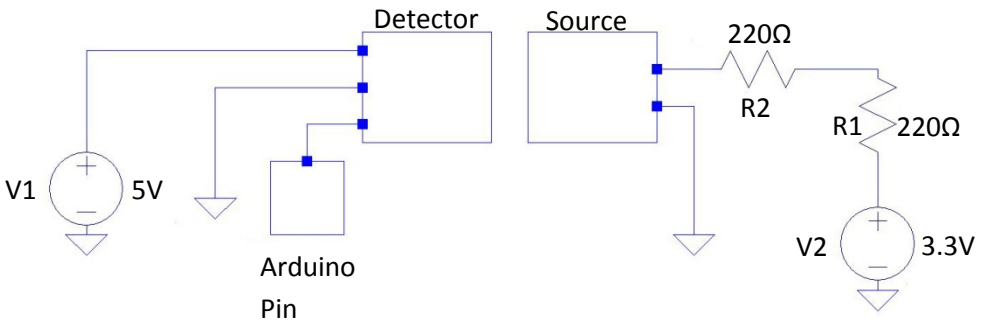

Figure 46: Wiring Diagram for the Photointerrupter.
This is the circuitry used for the device calibration. The detector and source are located inside the photo interrupter. The two input voltages and ground lines come from the Arduino.

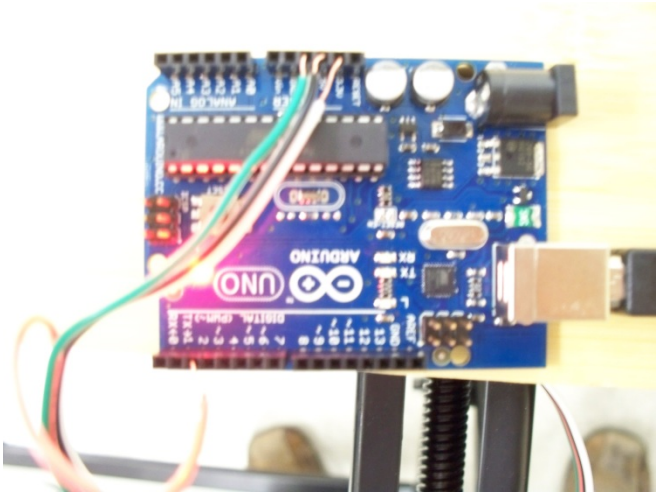

Figure 47: Wiring for the Photointerrupter onto the Arduino.
On the top from left to right: Ground, 5 Volts, 3.3 Volts; Bottom: Signal.